Karlsruhe Institute of Technology

CERN | EP-DT Detector Technologies

Process Optimization of a Selective Microstructured Nickel/Gold Metallization aimed at Topology Adaptation for the Hybridization of ASICs and Silicon Pixel Sensors

Master's Thesis

by

Moritz Lauser

Institute for Data Processing and Electronics (IPE)
at the
Faculty of Physics
at the
Karlsruhe Institute of Technology (KIT)

Supervising professor:	Prof. Dr. Frank Simon (IPE)
Supervising professor:	Prof. Dr. Ivan Peric (IPE)
Supervisor:	Dr. Dominik Dannheim (CERN)

Submission date: 7.January 2026

Statement of authorship

I declare under oath that I have written this master's thesis independently and exclusively using the literature and other resources listed. This thesis has not been submitted in the same or a similar form to any other examination authority for the purpose of obtaining an academic degree.

Karlsruhe, 07. January 2026

Moritz Lauser

Contents

Abstract 1

List of Acronyms 2

1 Introduction 3
- 1.1 Motivation . . . 3
- 1.2 Hybrid silicon pixel detectors . . . 4
- 1.3 Hybridisation . . . 4
  - 1.3.1 Solder/Indium Bumps . . . 6
  - 1.3.2 Copper Pillars . . . 7
  - 1.3.3 Anisotropic Conductive Adhesives . . . 8
- 1.4 Electroless Nickel Immersion Gold plating . . . 9
  - 1.4.1 Pixel topology . . . 9
  - 1.4.2 Plasma cleaning . . . 9
  - 1.4.3 Etching and Zincation . . . 10
  - 1.4.4 Nickel deposition . . . 10
  - 1.4.5 Immersion gold . . . 11

2 Methods and Materials 12
- 2.1 Samples used in this work . . . 12
- 2.2 Equipment for sample preparation and measurements . . . 14
- 2.3 ENIG process setup . . . 17
- 2.4 Materials . . . 18
- 2.5 Analysis of bump height and uniformity . . . 18

3 Results 20
- 3.1 Influence of pretreatment . . . 20
- 3.2 Influence of nickel deposition . . . 29
  - 3.2.1 Nickel deposition reference . . . 29
  - 3.2.2 Effect of temperature . . . 34
  - 3.2.3 Effect of pH value . . . 35
  - 3.2.4 Effect of stabilizer concentration . . . 36
  - 3.2.5 Effect of increased temperature and pH value . . . 39
- 3.3 Discussion of plating results . . . 40
- 3.4 Hybridisation of plated samples . . . 42
  - 3.4.1 Plating . . . 43
  - 3.4.2 Hybridisation . . . 44
  - 3.4.3 Functional measurements . . . 46
  - 3.4.4 Estimation of interconnect yield . . . 50

4 Conclusions and Outlook **51**

List of figures **55**

List of tables **56**

Bibliography **60**

Abstract

Hybrid silicon pixel detectors require a reliable interconnect technology to electrically and mechanically connect pixel sensors and readout electronics. As an alternative to conventional solder-based hybridisation, this work investigates a novel in-house hybridisation approach based on Anisotropic Conductive Adhesives (ACAs), which requires a specific protruding pixel pad topology. This topology is realised using a selective Elektroless Nickel Immersion Gold (ENIG) plating process on aluminium pixel pads. The focus of this thesis is the systematic optimisation of the ENIG process with respect to bump height, uniformity, and reproducibility. A detailed parameter study is conducted, analysing the influence of pretreatment, in particular the number of zincations, as well as nickel deposition temperature, pH value, stabiliser concentration and deposition time. The results show that the pretreatment is a key factor for achieving homogeneous nickel growth. Multiple zincations significantly improve surface uniformity and reduce roughness of the ENIG bumps. The nickel deposition rate is found to be parameter dependent in a range of 3-26 µm/h and can be precisely tuned by adjusting temperature and pH. Inappropriate stabiliser concentrations are shown to cause either parasitic nickel deposition on the passivation layer or premature termination of growth at pad edges. Based on the identified optimal process window, uniform ENIG bumps with well-controlled height are reproducibly achieved for samples without prior defects. Flip-chip assemblies using ACA and daisy-chain test structures demonstrate a high connection yield of up to 99%, confirming the suitability of the optimised ENIG process for fine-pitch hybridisation. The presented results show the potential of ENIG plating in combination with ACA as a flexible in-house solution for the hybridisation of pixel detectors, particularly for small-volume prototyping in research environments.

List of Acronyms

ACA	Anisotropic Conductive Adhesive. 1, 5, 8, 9, 42, 50, 51, 53
ACF	Anisotropic Conductive Film. 8, 18, 42, 43, 45
ACP	Anisotropic Conductive Paste. 8
AFM	Atomic Force Microscope. 16, 26–28, 51, 54
AIDAinnova	Advancement and Innovation for Detectors at Accelerators. 3, 12
ASIC	Application Specific Integrated Circuit. 3–7, 9, 43, 45, 53
CERN	European Organization for Nuclear Research. 3, 11
DRD3	Detector Research and Development 3 – Solid State Detectors. 3
EDS	Energy Dispersive Spectroscopy. 15, 20–25, 34, 53
ENIG	Elektroless Nickel Immersion Gold. 1, 3, 5, 9–12, 17–20, 24–28, 30–36, 41–51, 53, 54, 56
EP R&D	Experimental Physics - Research and Development. 3
FCBG	Fondation Campus Biotech Geneva. 14
FIB	Focused Ion Beam. 16, 32–34, 54
GUI	graphical user interface. 18, 19, 53
MPW	Multi Project Wafer. 12
PCB	Printed Circuit Board. 4, 53
ROI	region of interest. 18, 19
SEM	Scanning Electron Microscope. 6, 7, 15, 16, 20–27, 30–39, 51, 53, 54
UBM	Under Bump Metallization. 9, 51
WLI	White Light Interferometry. 16, 18, 19, 21

1 Introduction

This chapter outlines the broader context of the research to provide a foundation for the following chapters. It begins with a brief motivation of the investigated topic, followed by a short overview of hybrid silicon pixel detectors. Furthermore, existing hybridisation methods are discussed in detail and their strengths and weaknesses are highlighted. Finally, the hybridisation method examined in this thesis is introduced and the ENIG plating process required for it is explained.

1.1 Motivation

In order to precisely determine the underlying mechanisms of the creation and decay of particles in high-energy collider experiments, it is necessary to accurately measure the origin, the trajectory and the energy of the particles emerging from the collisions. This requires a series of detectors surrounding the primary interaction point, including high-resolution pixelated tracking detectors in the innermost layers. The development of advanced pixel detectors is therefore of fundamental importance for the future enhancement of tracking-detector systems.
Hybrid silicon detectors made of separate layers of pixelated sensors and readout Application Specific Integrated Circuits (ASICs) are widely used in high energy physic tracking detectors, due to their high performance and robustness against radiation [1]. The hybrid concept allows for an independent optimisation of the technologies and designs used for the respective sensing and readout layers, depending on the target application. These advantages have enabled the use of hybrid pixel detectors also in other fields, such as medical imaging, materials analysis, cultural heritage, space research, nuclear safety and education [2]. In the hybrid pixel detector approach, the two chips must be connected in a subsequent hybridisation step. This adds complexity and cost, and often requires specialised post-processing technologies only available for large-volume productions. An innovative and cost-effective new in-house hybridisation technology based on conductive adhesives is therefore under study [3]. This technology can be used for processing of individual dies, making it suitable in particular for small-volume productions during prototyping. The new hybridisation technique requires a specific topology of the pixel contact pads, which can be achieved using a newly developed in-house electroless Ni/Au (ENIG) plating process. This master's thesis focuses on optimising the ENIG process for this hybridisation technique.
The studies have been performed within CERNs strategic Experimental Physics - Research and Development (EP R&D) programme [4] and the DRD3 [5] and AIDAinnova [6] collaborations.

1.2 Hybrid silicon pixel detectors

Figure 1.1 shows a schematic representation of a hybridised assembly of a sensor and a readout ASIC on a Printed Circuit Board (PCB). The sensor part consists of an array of silicon diodes (pixels), which are operated in reverse bias mode to deplete the silicon bulk from free charge carriers and create an electric field between the sensor backside and the readout electrode at the p-n-junction [7]. When a particle passes through the sensor, it ionises the sensor material, generating electron-hole pairs. The generated electron-hole pairs are separated by an applied electric field. This generated current is conducted to the readout electronics via electrical connections. In Figure 1.1, this is achieved by solder bumps. This current is then processed by the readout chip to produce digital hit-data confirming the position and time at which the particle passed.

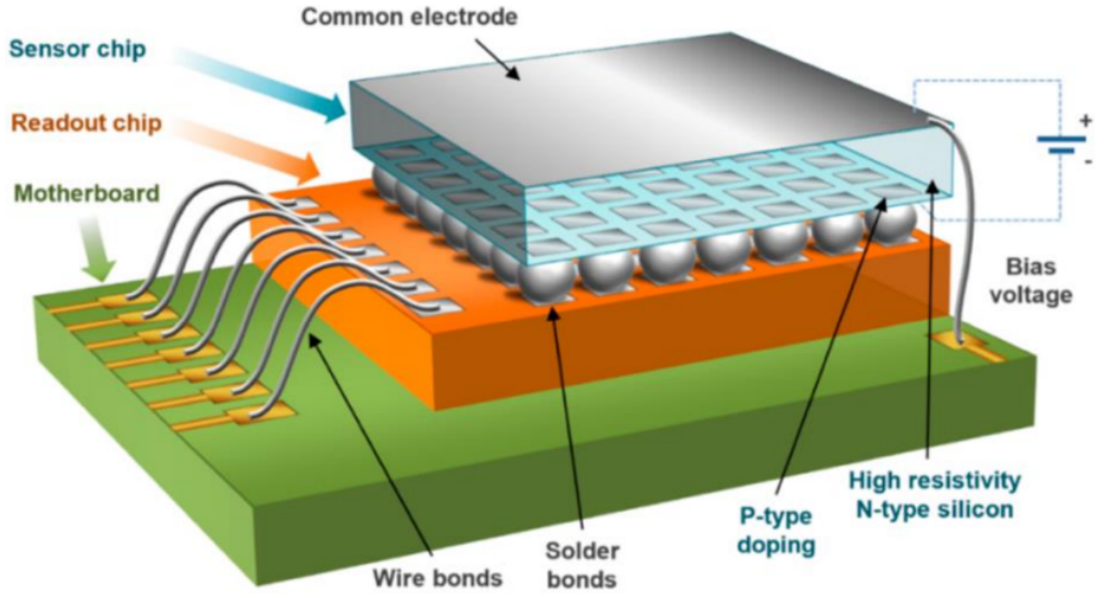


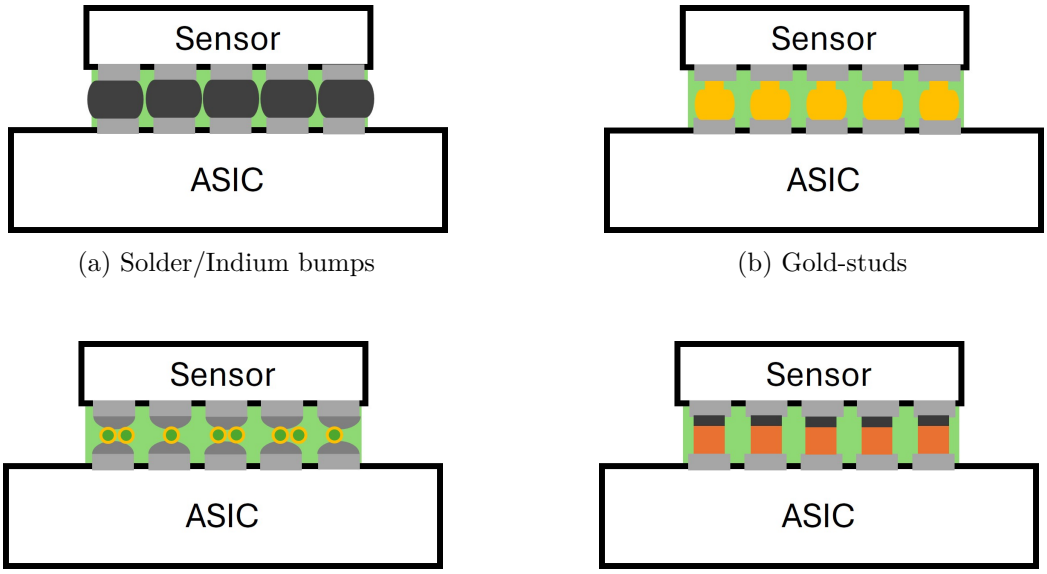
Figure 1.1: Schematic image of a hybrid pixel detector consisting of a silicon sensor on top bump-bonded to a readout ASIC below. The hybrid of sensor and ASIC is wire-bonded onto a "Motherboard" PCB. From [8].

1.3 Hybridisation

The construction of hybrid pixel detectors necessarily involves hybridisation. There are several different methods of hybridisation. Each method has advantages and disadvantages. The most common types of hybridisation are presented below for comparison with the chosen hybridisation method in this thesis.
In pixel detectors, hybridisation refers to the process by which two functionally different but complementary semiconductor structures are connected mechanically and electrically (in the case of this thesis, the sensor and the ASIC). To transmit the signal from the sensor to the ASIC, there are electrical input or output points on both chips called pads. Through the hybridisation, an electrical connection must be created between the pads of both chips. This creates a hybridised

pixel detector, in which each pixel of the sensor is connected to a corresponding readout channel. There is a trend towards achieving a higher density of pixels per area, using production processes with decreasing feature sizes. This leads to better spatial resolution. However, it also poses a major challenge in terms of hybridisation, as it is becoming increasingly difficult to scale down the interconnect technology accordingly. Research is being conducted into different methods to address this issue and to apply existing methods to smaller pitches [9].

Solder bumps are used for a wide range of pitches. If indium is used instead of solder, even ultra-small pitches of 5 µm are possible [10]. Gold studs created individually using a ball-wedge bonder are used mainly for low-density interconnects due to the comparably long processing times, but have also been applied to small pitches down to 55μm. Copper pillars are used for fine pitches well below 50 μm.
As an alternative to conventional hybridisation methods, this work investigates ENIG bumps in combination with ACA.



(a) Solder/Indium bumps

(b) Gold-studs

(c) Anisotropic conductive adhesives (ACA)

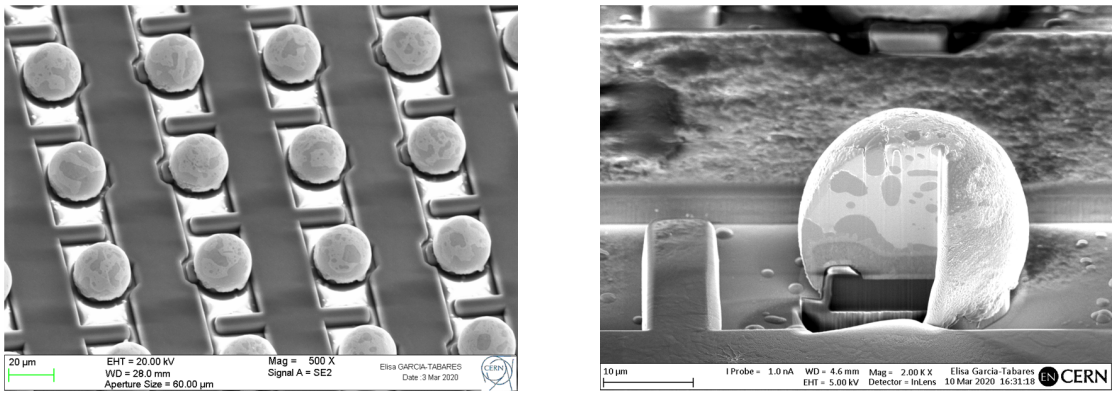
(d) Copper pillars

Figure 1.2: Schematic representation of hybrid pixel sensors using different hybridisation methods.

After the bumps have been applied, the sensor and ASIC are brought into contact using a flip-chip process. For this, the sensor is positioned precisely above the ASIC and permanently connected via either solder reflow or thermo-compression. Figure 1.2 shows schematic representations of hybridised sensors and ASICs using different methods. The pads of the sensors and ASICs are shown in grey. Depending on the hybridisation method used, a different electrically conductive connection is formed. Mechanical stability can be enhanced by an adhesive, which is typically injected post-process as an underfill, if necessary.
The various hybridisation methods involving solder or indium bumps, copper pillars and ENIG in combination with ACA are presented in more detail below.

1.3.1 Solder/Indium Bumps

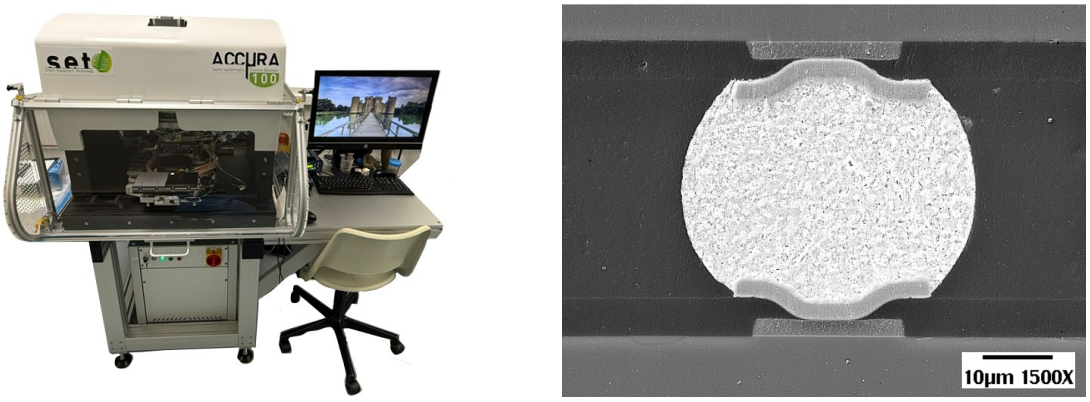
The industry standard for hybridising pixel detectors is currently to use solder bumps. The solder is often made from tin-lead or tin-silver alloys. Indium is used as an alternative to conventional solder when it fails due to mechanical or thermal issues. After the production of the ASICs, solder bumps are applied to the pads. The ASICs are then heated to melt the solder (reflow), while the sensor is brought in contact to the ASIC using a flip-chip machine. As the solder cools, it forms a stable connection between the ASIC pads and the sensor pads. This hybridisation method was pioneered by IBM in the 1960s under the designation "Controlled Collapse Component Connection" (C4) [11].



(a) Solder bumps on a Timepix3 after reflow. (b) Cross-section of one solder bump.

Figure 1.3: Scanning Electron Microscope (SEM) images of solder bumps on a Timepix3 ASIC.

The production of solder bumps involves lithography steps that require masks, making this method relatively complex and expensive. Moreover, these lithography steps have to be carried out at wafer level before the individual chips are separated. Figure 1.3 shows solder bumps on an ASIC. Figure 1.4 shows a flip-chip machine and a connection trough solder bumps after hybridisation.



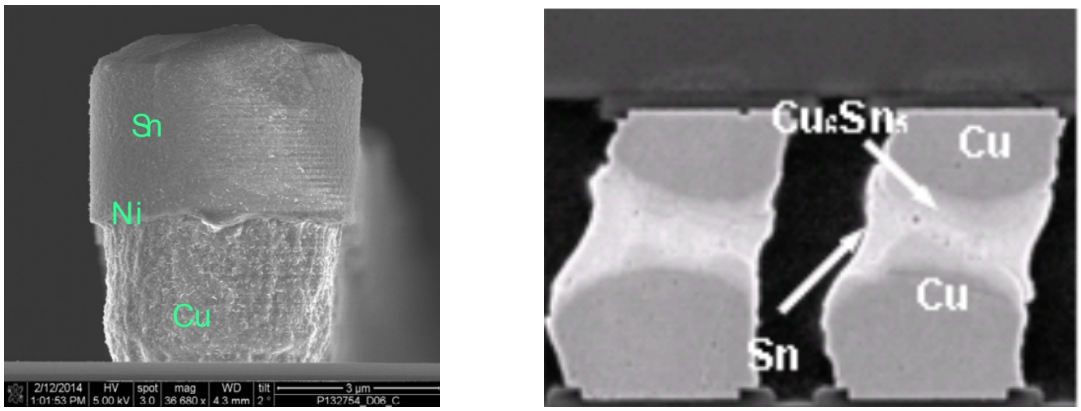
(a) Flip-chip maschine SET Accura 100. (b) Cross-section of a solder bump hybridisation [12].

Figure 1.4: Images of the used flip-chip machine for this thesis and an example solder bump connection after hybridisation.

While hybridisation with solder bumps are highly effective for commercial applications requiring thousands of identical assemblies, they present significant challenges for research environments where small quantities of diverse sensor-ASIC combinations must be prototyped and tested. This problem arises because the entire solder bump process is carried out at wafer level. For small quantities, which are often required in the development phase, the individual dies must be glued to a support wafer for processing. This results in high costs per hybrid. Solder bumps are capable of hybridizing pitches down to 25μm [13]. When indium is used, pitches of 5 µm are possible [10].

1.3.2 Copper Pillars

Copper pillars work in a similar way to solder bumps. One advantage is that they can be used to hybridise smaller pitches than solder bumps. To achieve this, copper columns are first applied to the pads using lithography processes and masks. A small amount of solder is then deposited on the pillars [14]. This solder is then reflown and brought into contact with the pads of the second chip, typically in an inert atmosphere to avoid oxidation of the contact surfaces. The positioning of the chips is realised by a flip-chip machine.
Figure 1.5 shows a copper pillar and a connection through a copper pillar after hybridisation. For the same reasons as with solder bumps, the process of manufacturing copper pillars is also carried out at wafer level.



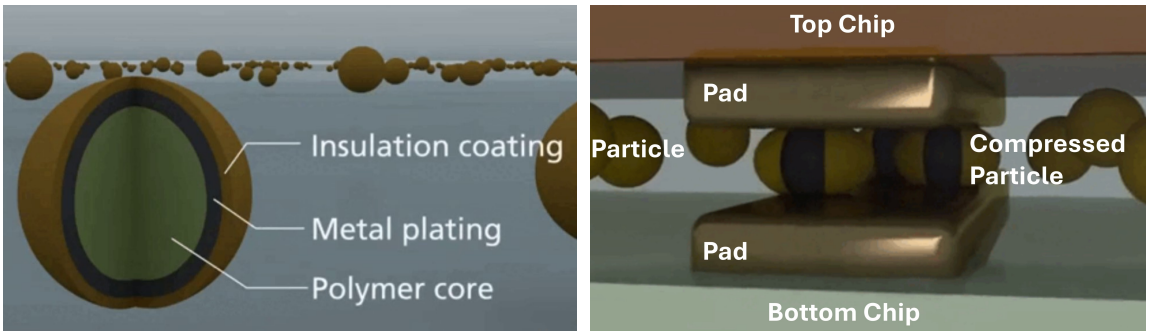
(a) SEM picture of a copper pillar [14]. (b) Cross-section of a copper pillar hybridisation [15].

Figure 1.5: Images of copper pillars.

Copper pillars allow a smaller amount of solder to be used for hybridisation because the copper already bridges part of the gap between the chips. The smaller amount of solder means that it does not spread as much across the surface, which prevents shorts and allows to hybridise chips with a smaller pitch, down to 15μm [15].

1.3.3 Anisotropic Conductive Adhesives

With Anisotropic Conductive Adhesives (ACAs), electrical contact is achieved using conductive particles instead of solder. ACA consist of a polymer resin into which conductive micro-particles, typically small metal or metal-coated polymer spheres of 3-30μm diameter, are embedded.
During the flip-chip hybridisation, an ACA film (Anisotropic Conductive Film (ACF)) or paste (Anisotropic Conductive Paste (ACP)) is applied between two contact surfaces and then cured under pressure and elevated temperature (thermo-compression).



(a) Schematic representation of ACA with microparticles [16].

(b) Schematic representation of hybridisation with ACA [16].

Figure 1.6: Schematic representations of ACA and the resulting electrical contact.

In the x/y plane, the ACA remains insulating because of the glue between the particles; in the z direction between the pixel pads, it is conductive due to the compressed particles making contact between the pads. Figure 1.6 shows schematic representations of ACA and how the anisotropic electrical contact is realised.
This anisotropic conductive property enables fine-pitch electrical contact with many pads simultaneously connected, preventing short circuits between neighbouring pads. ACA connections are particularly used for low-density interconnects in the display, sensor and 3D integration technology. The advantages of ACA connections are the suitability for single-die processing and fine pitch structures. Moreover, ACA connections are also suitable for sensitive materials due to the possible low bonding temperature ($\leq$100°C). Their higher contact resistance compared to metallic connections is a disadvantage.
ACA can be used as an alternative to solder for establishing electrical contact between pads, bumps, pillars and other structures. The achievable pitch depends on the size and density of the particles and the amount of adhesive used.
Hybridisation with ACA requires a pixel pad topology in which the pads protrude in order to compress the conductive particles as shown in Figure 1.6b. This topology must first be created on the pixel pads before hybridisation can take place.

1.4 Electroless Nickel Immersion Gold plating

This thesis uses Electroless Nickel Immersion Gold (ENIG) plating, to produce the protruding pixel pads required for hybridisation with ACA. For hybridisation, it is important that the height of the ENIG bumps on the pixels is as uniform as possible across the entire pixel matrix in order to achieve a high connection yield. With ENIG, nickel is first deposited on the aluminium pixel pads in a self-catalytic process. In the next step, the nickel is coated with a thin layer of gold. This makes the nickel layer corrosion-resistant.
More recently, attempts have been made to exploit the selectivity of the deposition to coat pixel pads [17]. This is particularly challenging with small pitches and small pads.
Another advantage of ENIG is that the gold layer has good contact angle properties with solder. This is why ENIG is often used as a so-called Under Bump Metallization (UBM). Solder wets the gold and thus remains locally on the pad, which reduces the risk of it flowing away and causing shorts during hybridisation.
The process steps required for ENIG are briefly introduced in the following. More details will then be presented in chapters 2 and 3.

1.4.1 Pixel topology

Figure 1.7 shows a schematic representation of one pixel in an untreated sensor or ASIC chip. A passivation layer (often a double layer of SiO_2 and Si_3N_4 is used) protects the surface of the chip. Openings of the passivation layer above each pixel pad give access to the exposed aluminium pad metal. The surface usually contains organic contaminants and has an oxide layer on the aluminium pads.

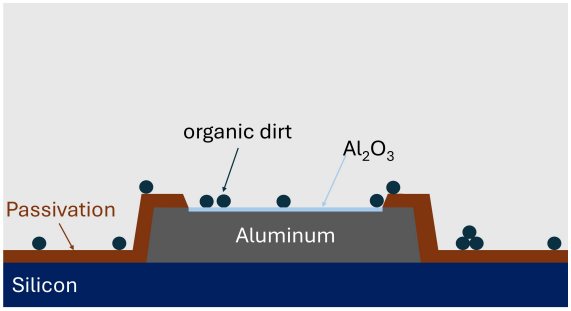
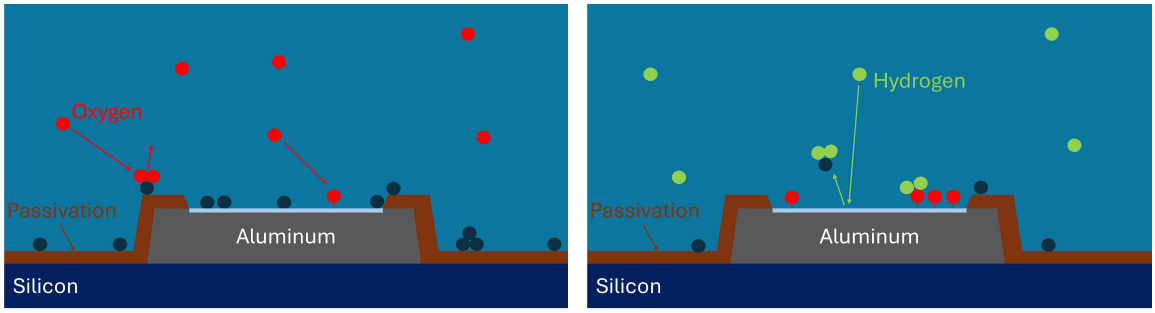


Figure 1.7: Schematic representation (cross-section view) of a sensor or ASIC pixel containing surface contamination.

1.4.2 Plasma cleaning

Plasma cleaning is used to remove organic contaminants. In Figure 1.8a and 1.8b, the surface is first cleaned with a mixture of argon/oxygen and argon/hydrogen plasma. The oxygen or hydrogen radicals react with organic compounds, causing them to transition into the gas phase. In addition, oxygen accumulates on the surface, which improves the wettability of the surface.

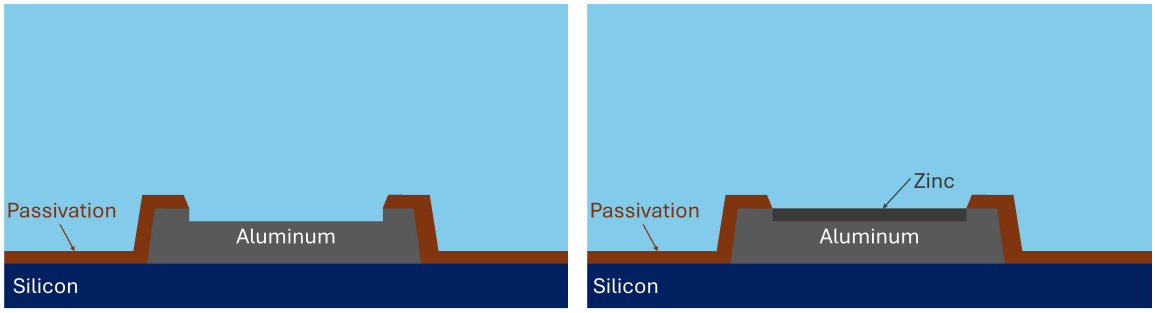


(a) Oxygen plasma. (b) Hydrogen plasma.

Figure 1.8: Schematic representation of treatment with plasma.

1.4.3 Etching and Zincation

The aluminium and any remaining aluminium oxide are then etched away so that zinc can be applied to the aluminium. These processes are illustrated schematically in Figure 1.9. The zinc is necessary to act as a reaction starter in the following step. After applying the zinc layer, a stripper is often used to remove all or part of the zinc. Zinc is then reapplied, removed again and reapplied once more. This process improves the uniformity of the zinc layer.



(a) Aluminium etching. (b) Zinc deposition.

Figure 1.9: Schematic representation of etching of the aluminium and the deposition of zinc.

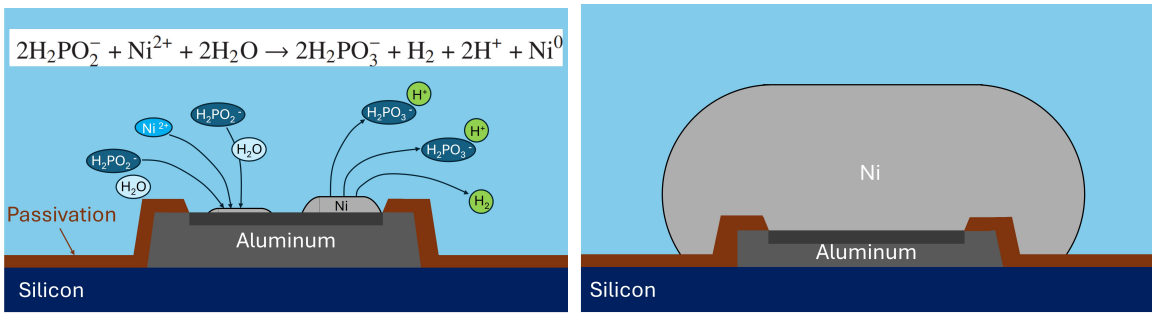
1.4.4 Nickel deposition

Nickel is initially deposited onto the zinc in a wet-chemical process, to form the bulk material of the ENIG bumps. The nickel deposition is self-catalytic and grows isotropically with time according to the chemical reaction:

$$2H_2PO_2^- + Ni^{2+} + 2H_2O \rightarrow 2H_2PO_3^- + H_2 + 2H^+ + Ni^0 \tag{1.1}$$

The deposition mechanism of nickel and a nickel bump after a certain exposure time are illustrated schematically in Figure 1.10. The shape of the resulting nickel bump is influenced by the geometry of the pad, the height of the aluminium and the height of the passivation. To prevent shorts

between neighbouring pixels, the nickel bumps on neighbouring pixels must not overlap. Since growth is isotropic, this requirement limits the height in relation to the pitch and passivation openings of the chips.



(a) Nickel deposition starts. (b) Nickel deposition after some time.

Figure 1.10: Schematic representation of nickel deposition.

1.4.5 Immersion gold

The final immersion gold step is intended to make the nickel bump corrosion-resistant and also has the advantage of good wettability of gold. For this purpose, an exchange reaction takes place in the first atomic layers between nickel atoms and gold atoms. This results in a thin gold coating. This process is illustrated schematically in Figure 1.11.

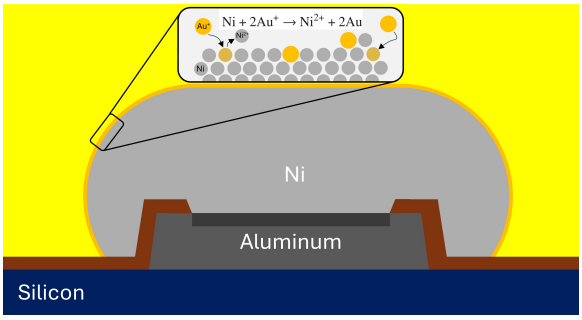


Figure 1.11: Schematic representation of immersion gold bath.

The ENIG process needs to be precisely adjusted for the respective pixel pitch and matrix area, to achieve a sufficient plating height and uniformity across the pixel matrix.
Research has already been conducted at CERN to develop an in-house ENIG plating process [18, 19, 20, 21]. This thesis aims to build up on this prior work and present a systematic determination of the influence of individual parameters during processing. These findings are used to optimise the processing method, predict the ENIG bump height and uniformity for different geometries and chips made of different materials.

2 Methods and Materials

This chapter provides an overview of the samples used, as well as an introduction to the equipment and chemicals employed. It then presents the software that was developed to analyse height and height distribution. This software was used to determine the results presented in chapter 3.

2.1 Samples used in this work

In order to optimise ENIG plating, this work makes extensive use of daisy chain devices. In addition to analysing the plating, these can also be used to estimate the connection yield after hybridisation. Devices from an AIDAinnova daisy chain production in 2022 are used for this purpose [22]. This Multi Project Wafer (MPW) contains a variety of designs with different pitches and matrix sizes, as shown in Figure 2.1.

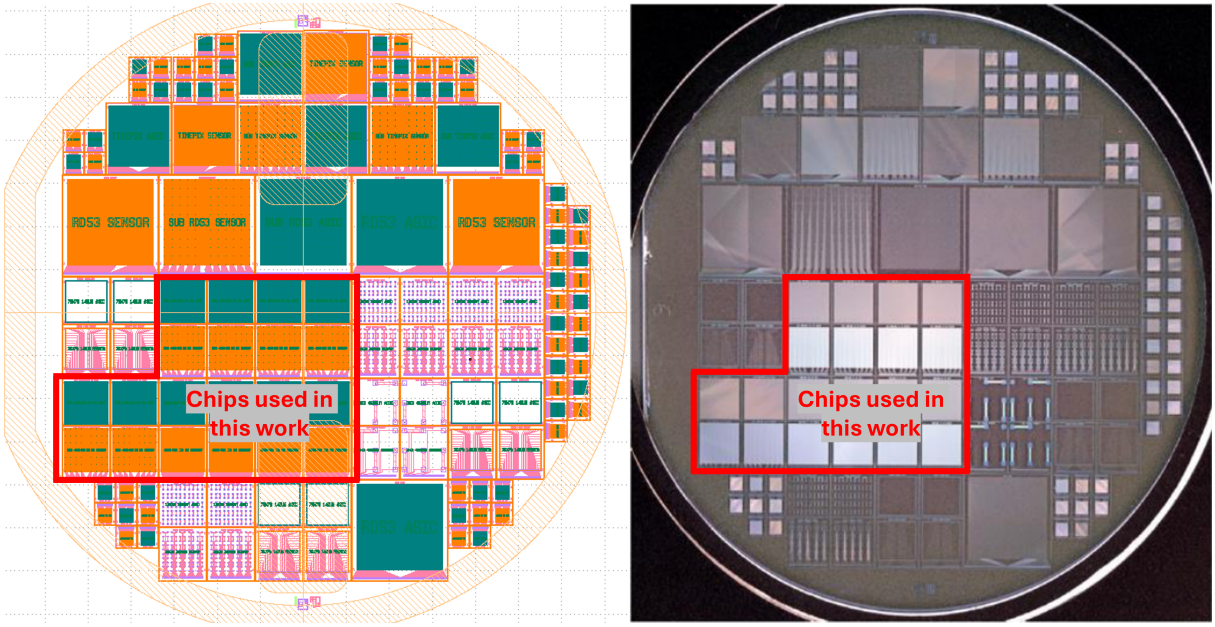


Figure 2.1: Dimensions and positioning of the individual devices on the wafer, as well as an actual image of the wafer after manufacture [22].

The selected daisy chain devices have a matrix size of 400x400 and a pitch of 25 μm. These devices are outlined in red in Figure 2.1. They have a single patterned metal layer made of aluminium with a thickness of 2.5 µm on a quartz substrate with a thickness of 625 µm. The passivation layer has a thickness of 950 nm. The samples used for the results in section 3 come from five

different wafers of this type. The devices are designed in such a way that chains are formed after hybridisation, which can then be tested for electrical resistance.

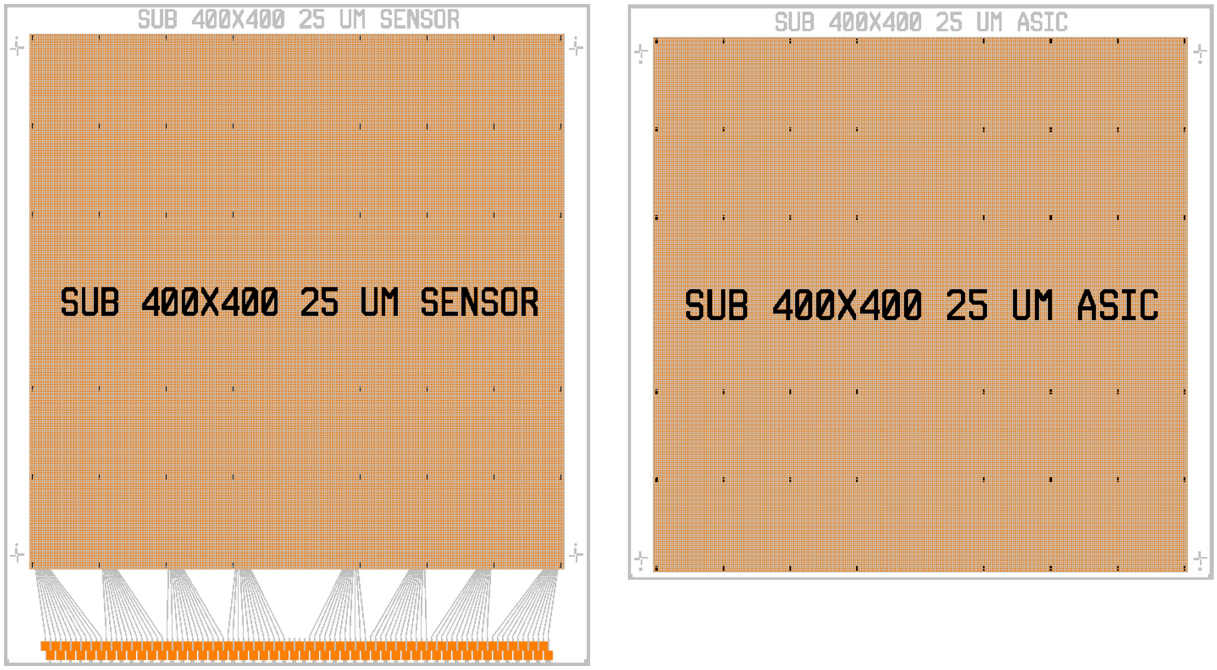
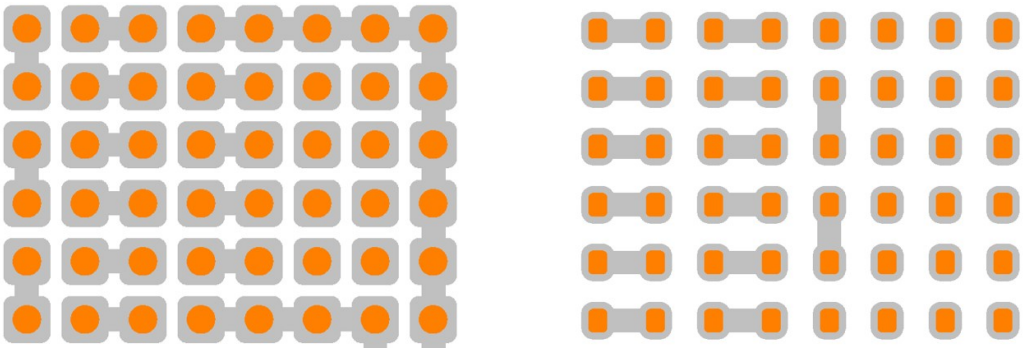


Figure 2.2: Visualisation of the design of the two matching devices.

Figure 2.3 shows the layout of the matching pair of devices. Both devices have a matrix area of 1 mm x 1 mm. The first device has a length of 1.235 mm and a width of 1.095 mm. The contact pads used to measure resistance are visible in the lower section. The other device has a length of 1.075 mm and a width of 1.095 mm. The crosses in the corners of the two devices are used later to validate the alignment after hybridisation. The black dots on both devices illustrate the locations of the chains islands. A total of 48 islands are distributed across the surface of both devices. Figure 2.3 shows one of the corresponding island locations for each device greatly enlarged.



(a) Visualisation of an island of the 'SUB 400x400 25UM Sensor'.

(b) Visualisation of an island of the 'SUB 400x400 25UM ASIC'.

Figure 2.3: Visualisation of individual islands of the two daisy chain devices.

Figure 2.3a shows an island of the 'SUB 400x400 25UM Sensor' device. This includes the chain area and the connecting lines that lead to the contact pads in the periphery. Figure 2.3b shows an island of the 'SUB 400x400 25UM ASIC' device. This only contains the chain area. The entire matrix area between the islands is filled with unconnected dummy pixels that play no role in determining the connection yield.

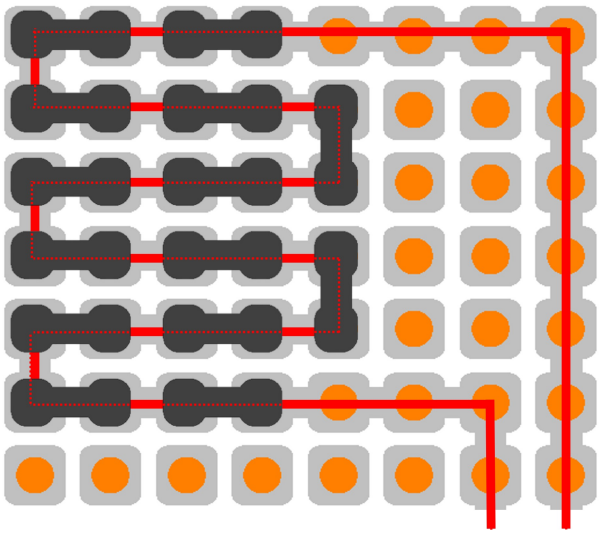


Figure 2.4: Schematic representation of the island after hybridisation, the resulting chain and the electrical connection shown as a red line.

When the devices are hybridised, they form an electrically connected chain. For these chains to function, 28 vertical connections must be made in series. Figure 2.4 shows a schematic representation of the resulting chain, with the electrical path marked in red. These connection lines lead to the lower end of the 'SUB 400x400 25UM Sensor' device, where they terminate in the contact pads.

2.2 Equipment for sample preparation and measurements

The following section briefly introduces the equipment used in this work for sample preparation and measurements, as well as there accuracies or resolutions.

Femtosecond laser

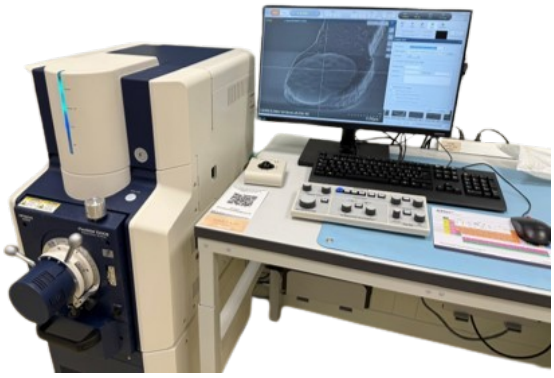
The daisy chain devices were separated using a laser dicer (WS-Turret MM200-USP [23]) in Fondation Campus Biotech Geneva (FCBG). The laser has micrometer-precision. Following laser ablation along the separation lines, the devices are broken by hand. An image of the machine is shown in Figure 2.5a.



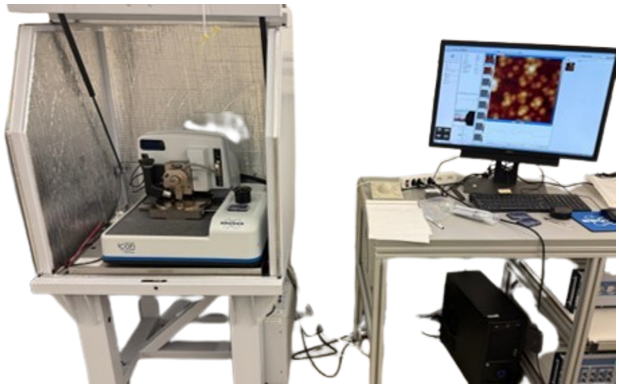
(a) WS-Turret MM200-USP laser dicer [23]



(b) HPT-500 Benchtop Plasma Treater



(c) FlexSEM 1000 Scanning Electron Microscope



(d) Dimension Icon Atomic Force Microscope

Figure 2.5: Various equipment used for the sample preparation and inspections.

Plasma Cleaner

The surfaces of the devices were treated with plasma. The HPT-500 Benchtop Plasma Treater from Henniker-Plasma [24], shown in Figure 2.5b, was used for this purpose. Mixtures of Ar/O_2 (80/20) and Ar/H_2 (98/2) were used.

Light Microscope

The VHX-6000 digital microskope from Keyence was used to take light microscope images, enabling up to 6000x magnification [25]. In addition to different light settings, it also allows for stitching images and taking images from an angle of up to approximately 60°.

Scanning Electron Microscope / Energy Dispersive Spectroscopy

The FlexSEM 1000 II from Hitachi High-Tech [26] was used to take high-resolution images. This enables SEM images to be taken at angles of up to 90° as well as Energy Dispersive Spectroscopy (EDS) images that detect different elements. The machine is shown in Figure 2.5c.

White Light Interferometry

The ContourX-100 White Light Interferometry (WLI) from Bruker was used for optical height measurements [27]. It has a resolution in the nanometre range. This machine also allows stitching images to be taken over larger areas.

Atomic Force Microscope

The Dimension Icon Atomic Force Microscope (AFM) from Bruker was used for high-resolution height measurements in the single-digit nanometre range [28]. It has a scan range of up to 90 µm and can therefore examine larger areas. A picture of the machine can be seen in Figure 2.5d.

Focused Ion Beam

The FIB-SEM XB 540 from Zeiss was used to capture the cross-sectional Focused Ion Beam (FIB) images. This enables material to be removed locally using an ion beam. The resulting cross-section can then be examined in high resolution using an SEM. An image of the machine is shown in Figure 2.6a.



(a) FIB-SEM XB 540 Zeiss [29]

(b) PA200 probe station.

Figure 2.6: Equipments used for the sample inspections.

Flip-chip machine

The SET Accura 100 flip-chip machine was used to hybridise the devices [30]. It enables hybridisation under pressures of up to 100 kgf and temperatures of up to 400°C. It has a positioning accuracy of approximately ±0.5 µm and a planarity of better than 100 µrad. A picture of the machine is shown in Figure 1.4a.

Probe station

A Karl Suss PA200 semi-automatic probe station was used to determine the connection yield of the hybridised samples. Figure 2.6b shows an image of the machine. Using a microscope and micro positioners, electrically conductive needles can be positioned on the pads of the samples with micrometer precision. This process is highlighted by the red boxes in the picture. Live images enable the positioning of needles and chuck, as well as validating needle contact, which is highlighted by the green boxes. A multimeter was used in a 2-wire connection to apply direct current to the needles and measure the resistance. The current flows through the needles via the contact pads and the connection lines to the islands. If hybridisation has occurred, the current flows through the island and the second connection line back to the contact pad, and then via the second needle back to the multimeter. This makes resistance measurable when the island is connected. Otherwise, the resistance is infinite. The multimeter is highlighted by the blue boxes.

2.3 ENIG process setup

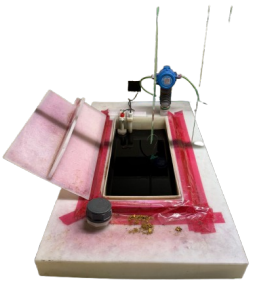
A wet-chemical setup was used to treat the samples with the ENIG process. Pretreatment (oxide removal and zincation) takes place in a clean room in beakers under ultrasound, as shown in Figure 2.7a. Nickel deposition takes place in the same fume hood in the clean room on a hotplate where the temperature and rotation speed can be adjusted. The hotplate measures and adjusts the temperature simultaneously. To minimise evaporation, the beaker is covered during nickel deposition. Figure 2.7b shows an image of the nickel deposition setup. The immersion gold step does not take place in the clean room; it is part of a process line in which solutions are centrally prepared for a longer period of time. Figure 2.7c shows an image of the immersion gold setup.



(a) Pretreatment setup in beakers with ultrasound.



(b) Nickel deposition setup on hotplate.



(c) Immersion gold setup in large tank

Figure 2.7: Setups used for this thesis for the entire ENIG process.

2.4 Materials

Ready-to-use solutions were purchased from Atotech [31] and mixed for ENIG processing. XENOLYTE Conditioner ACA2 Parts A and B, XENOLYTE AL Etching MA and XENOLYTE Zincate CFA were used for the pretreatment stage. Additionally, 60 percent nitric acid was employed as a stripper to remove zinc during several zincation steps.
Nickel deposition was achieved using XENOLYTE Nickel Make-up HP, XENOLYTE Nickel Solution HP and XENOLYTE Nickel Stabiliser C. The pH value was adjusted by adding ammonia acid at a concentration of 24.5 percent.
Aurolectroless SMT Make-up Solution and Aurolectroless SMT Gold Salt were used for the immersion gold bath.
Hybridisation was performed using the ACF HDF9032CP from H&S HighTech. It is 9±2 μm thick and the embedded micro particles (diameter 3±0.25 μm) consist of a polymer core coated with nickel and gold. The surface of the particle has spines and an insulating coating to prevent short circuits caused by connections across multiple pixels. The density of particles is 18.000±1.000 pcs/mm^2.

2.5 Analysis of bump height and uniformity

The Contourx-100 from Bruker is used to measure the height of the resulting ENIG bumps. In order to obtain more statistics in the evaluation method, instead of manually evaluating a few bumps in the Vision64 software, a programme was written in Python using the AI-Assistant Cursor [32] that takes into account many bumps and also the height changes on individual bumps. To do this, the OPD-file generated by the WLI must be converted into an ASCI-file. This allows the open source software Gwyddion [33] to read the data, correct it for tilt and then save it in a txt-file. This txt-file can then be read by the custom-developed analysis programme. This process flow is illustrated in Figure 2.8.

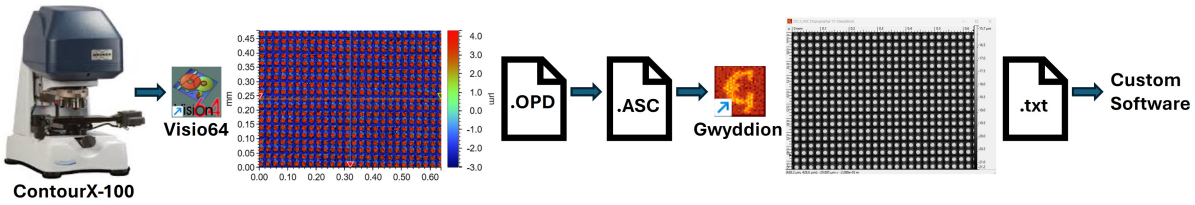


Figure 2.8: Process workflow for generating txt-files for height measurements.

Figure 2.9 illustrates the various sections of the graphical user interface (GUI) that is used to control the analysis programme. In the top left corner, height data is displayed graphically alongside a height legend. In the top right corner, the user controls the parameters of two region of interest (ROI). These ROIs can also be seen in the graphic display at the top left. The first ROI consists of red circles. The position, distance, number of circles per row and column, as well as their diameter and angle of rotation around the bottom left circle can be set. These settings allow for precise positioning of the circles over the ENIG bumps. The second ROI are blue rectangles. For these, the position, number of rectangles per rows and column, the distance and the size of

the rectangles can also be set. The blue rectangles are positioned on the passivation layer between the ENIG bumps. The programme automatically determines the height values within the two different ROIs and displays them in a histogram at the bottom left. The histogram and graphical ROI representation make it easy to validate the positioning. The height of the bumps can be determined by the difference in height values between the two ROIs. The standard deviation of the ENIG bump height values can be determined by the width of the red ROI distribution. The height values of the ENIG bumps in relation to the median height of the passivation layer can be written to a txt-file and named at the bottom right of the image. If the passivation layer is permeable to light (which is the case with the samples used), the WLI measures the underlying layer, which must be taken into account in the interpretation.

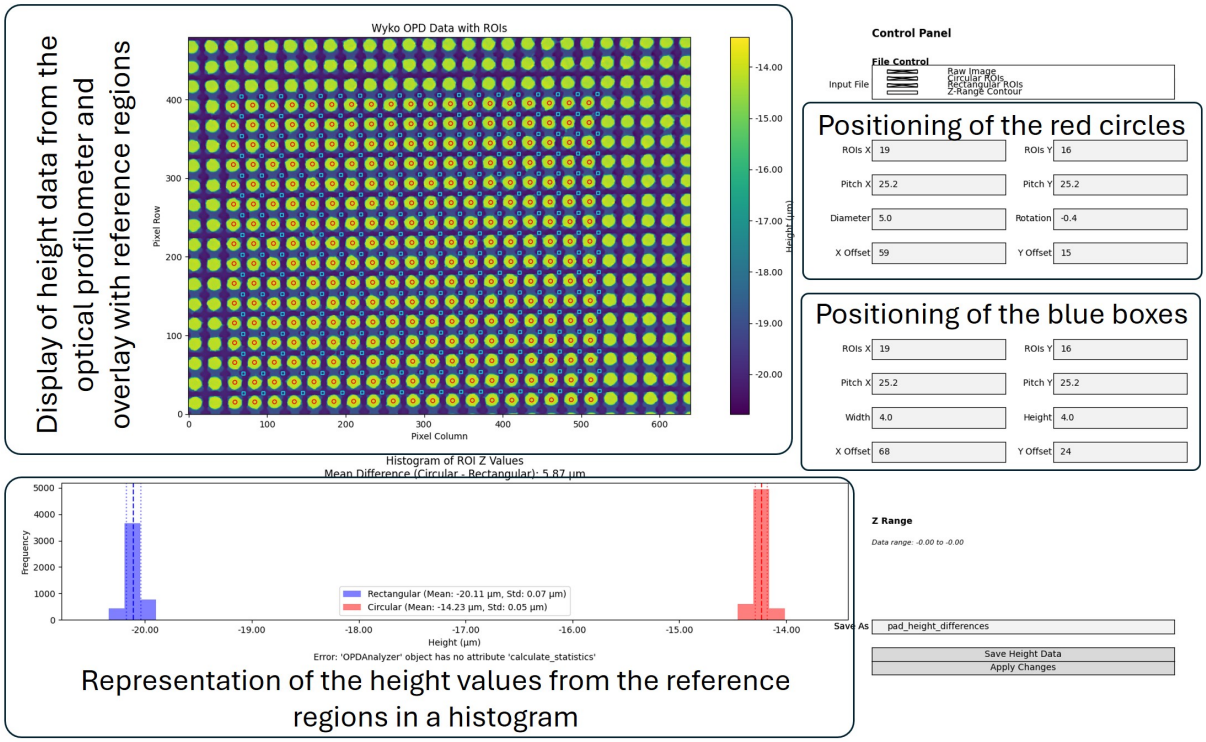


Figure 2.9: Display of the GUI of the custom developed analysis software.

This method generates about 6000 measurements from the pixels in the red ROI. These height measurements were cross-validated with manual measurements, yielding statistically validated results. This programme was used to obtain the ENIG bump height and uniformity results for Chapter 3, for which this workflow was performed at four corners and in the centre of the matrix.

3 Results

This chapter presents the results of the ENIG parameter-optimisation study as well as flip-chip results. The ENIG process is examined in detail at various stages. First, the observed relationship between the uniformity of a single ENIG bump and the pretreatment parameters are presented. Next, the influence of individual parameters on the deposition rate and uniformity across the pixel matrix during nickel deposition are discussed. Finally, the connection yield after flip-chip hybridisation is presented.

3.1 Influence of pretreatment

In the pretreatment step, the chip is prepared for ENIG plating. As nickel does not deposit on aluminium, an intermediate zinc layer is required. This section demonstrates the impact of the pre-treatment process on ENIG plating. The pre-treatment recipe consists of seven steps, listed in Table 3.1. In a series of experiments, six daisy chain samples described in section 2.1 were subjected to different pre-treatments before being treated with the same ENIG plating. The samples were then compared in terms of plating topology and uniformity across the matrix.

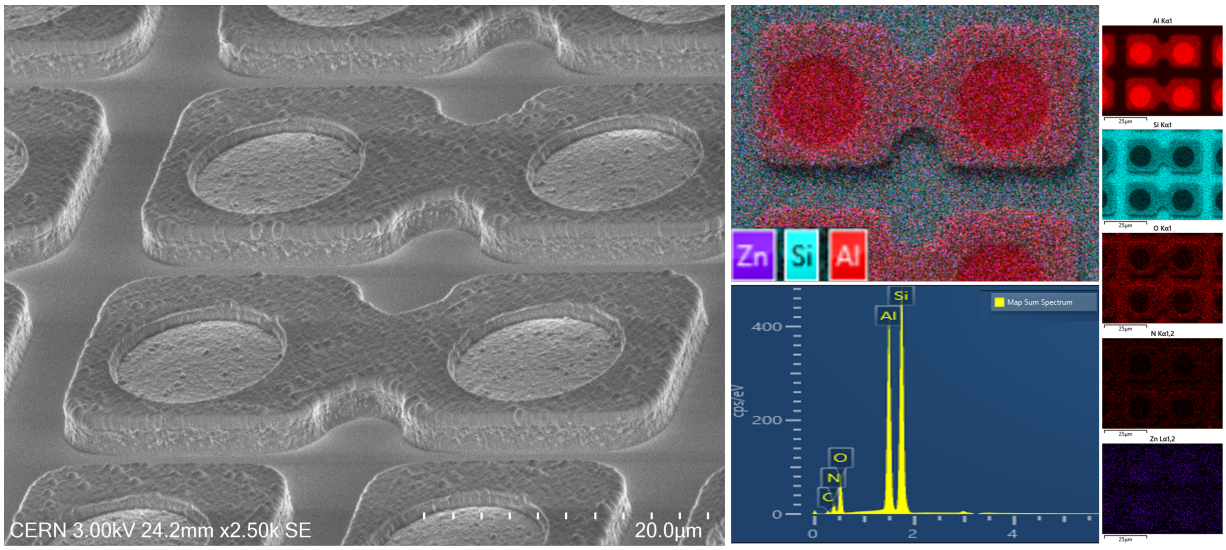


Figure 3.1: SEM image of one of the six samples and corresponding EDS analysis showing the composition of elements on the sample surface.

The six samples were examined prior to treatment. Figure 3.1 shows an SEM image and EDS analysis of one of the samples, which consist of structured aluminium deposited on a quartz wafer.

The passivation layer consists of a double layer of silicon oxide and silicon nitride and has round openings on the aluminium pads. In the EDS analysis, aluminium is shown in red and silicon in light blue. The passivation opening is also visible in the EDS analysis due to the higher aluminium signal. In the circle where the red is more intense, the aluminium signal is not shielded by the passivation.
In addition, the roughness of the aluminium layer was determined by measuring the uniformity of the height on the pads on each of the six different samples using a WLI and the programme described in section 2.5. Figure 3.2 shows the standard deviation of the measured height values. All six samples exhibit a low standard deviation of the aluminium pad of less than 0.1µm prior to treatment. Sample one has a higher standard deviation of around 0.08µm, while the other samples have a similar standard deviation of around 0.04µm.

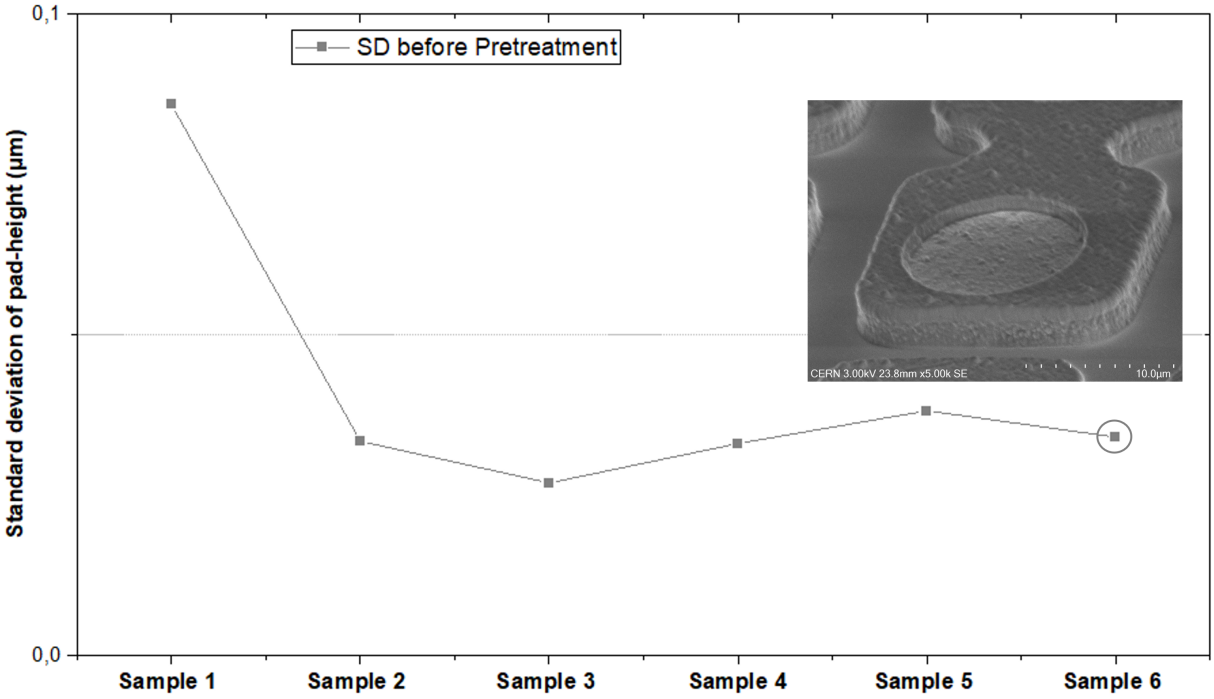


Figure 3.2: Measurements of the roughness of the exposed aluminium on all six samples and exemplary SEM image of one pad from sample 6.

The six samples were treated to varying degrees using the pretreatment recipe in Table 3.1. Sample 1 was exclusively treated with the cleaning and aluminium etching steps. Sample 2 underwent the cleaning, aluminium etching and first zincation steps. One additional step was added to each sample until the sixth sample, which underwent all steps up to the third zincation. All steps were carried out at room temperature in a beaker under ultrasound.

Table 3.1: Pretreatment step, Make-up solution and parameter

No.	Process	Make-up	Parameter
1	Cleaning	10% Cond. Part A, 10% Cond. Part B, 80% water*	2 min, RT**
2	Al Etching	50% Al Etch MA, 50% water*	2 min, RT**
3	First zincation	50% zincate, 50% water*	45 sec, RT**
4	Zinc removal	50% ammonia acid (c=24.5%), 50% water*	30 sec, RT**
5	Second zincation	50% zincate, 50% water*	45 sec, RT**
6	Zinc removal	50% ammonia acid (c=24.5%), 50% water*	30 sec, RT**
7	Third zincation	50% zincate, 50% water*	45 sec, RT**

water* = de-ionized water; RT** = Room temperature; the percentages (%) are shown by volume.

Subsequently, SEM images of the samples were taken again. An exemplary SEM image and the EDS analysis can be seen in Figure 3.3 for sample 2 that was treated up to the first zincation step. Round grains are visible on the SEM image that were not previously visible in Figure 3.1. In the EDS analysis, aluminium is again shown in red and silicon in light blue. The EDS analysis clearly shows that the round balls are zinc grains, which are shown in purple.

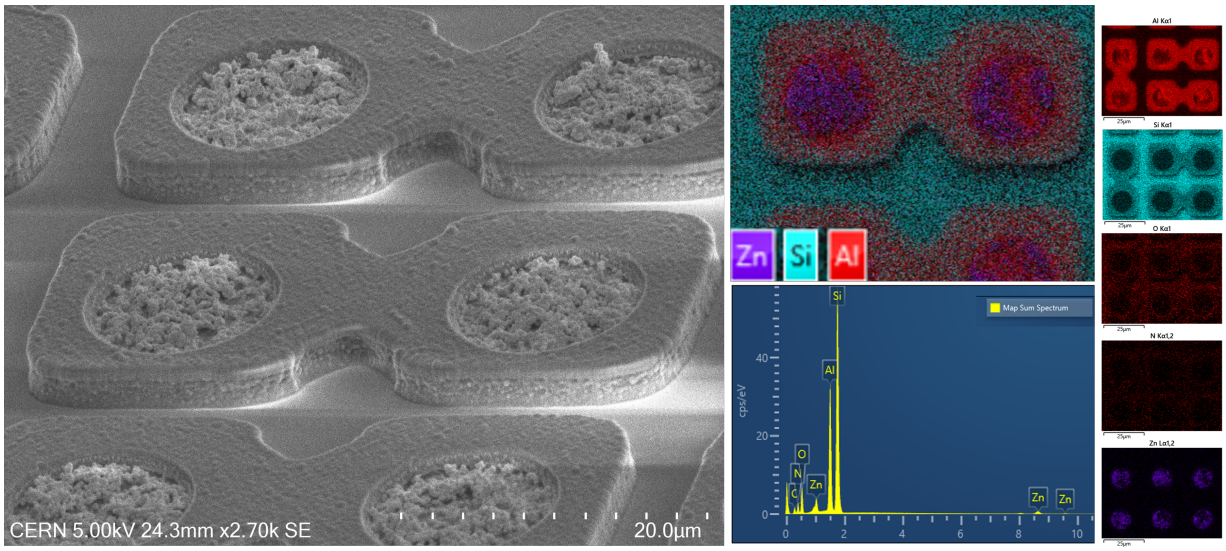
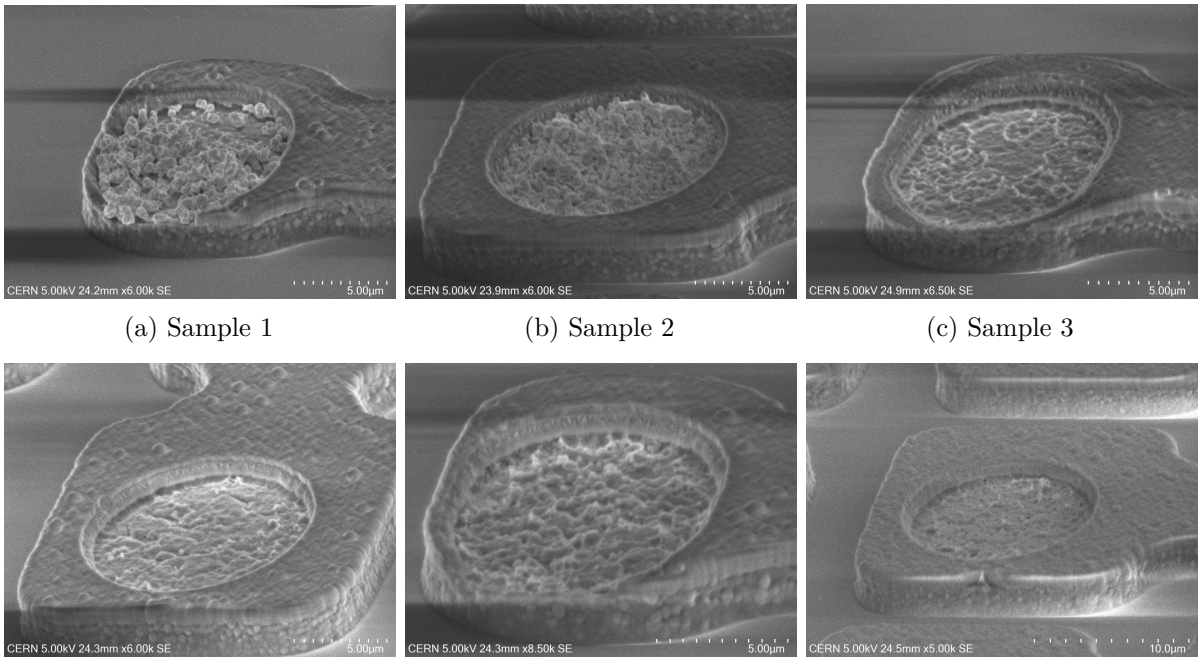


Figure 3.3: SEM image of Sample 2 after Pretreatment and corresponding EDS analysis.

An EDS analysis was performed on all six samples. The zinc content was very low or zero in all samples. Sample 1 contained 2.77% zinc; sample 2, 2.84%; sample 3, 0%; sample 4, 0.09%; sample 5, 0%; and sample 6, 0.24%. These percentages cannot be compared directly because the section of the image being measured is different, which would result in different percentages for the same amount of zinc per pad.



(a) Sample 1 (b) Sample 2 (c) Sample 3

(d) Sample 4 (e) Sample 5 (f) Sample 6

Figure 3.4: SEM images of samples 1-6 after their respective pretreatment.

Figure 3.4 shows SEM images of all six samples after their respective pre-treatments. Notably, sample 1 exhibits zinc grains after cleaning and aluminium etching, despite the absence of a dedicated zincation step. This is unexpected and could be caused by impurities. To rule out the formation of zinc due to contamination, a second sample identical to sample 1 was treated. This sample also had zinc on the aluminium pad after pretreatment, indicating that contamination might not the cause.
In sample 2, the zinc balls are clearly visible and are distributed more evenly across the aluminium pad than in sample 1. However, the surface still looks quite rough, similar to sample 1.
In samples 3 to 6, the zinc balls are no longer visible. However, since zinc was detected using EDS analysis, it is assumed that samples 4 and 6 still contain zinc, which is so finely distributed that it no longer forms the easily visible ball structure.

The standard deviation of the height values on the pads of the six samples was then measured again. The standard deviations determined after pretreatment are shown in orange in Figure 3.5. For comparison, the standard deviation values before pretreatment are shown in grey. The pretreatment increased the roughness of all six samples on the aluminium pad. This appears reasonable, as the aluminium is etched in all samples and then at least one zincation step follows in all samples except sample 1. Both the aluminium etching and the zinc deposition increase the roughness of the sample. An increase in roughness is also visible in the images from Figure 3.4 compared to Figure 3.1. However, the increase in roughness is small. The standard deviation of the height values is less than 0.3 µm for all six samples. Samples 1 and 2 are the roughest, with values of just under 0.2 µm and 0.3 µm respectively, as seen in the SEM images. Samples 3–6 have a roughness of approximately 0.1 µm.

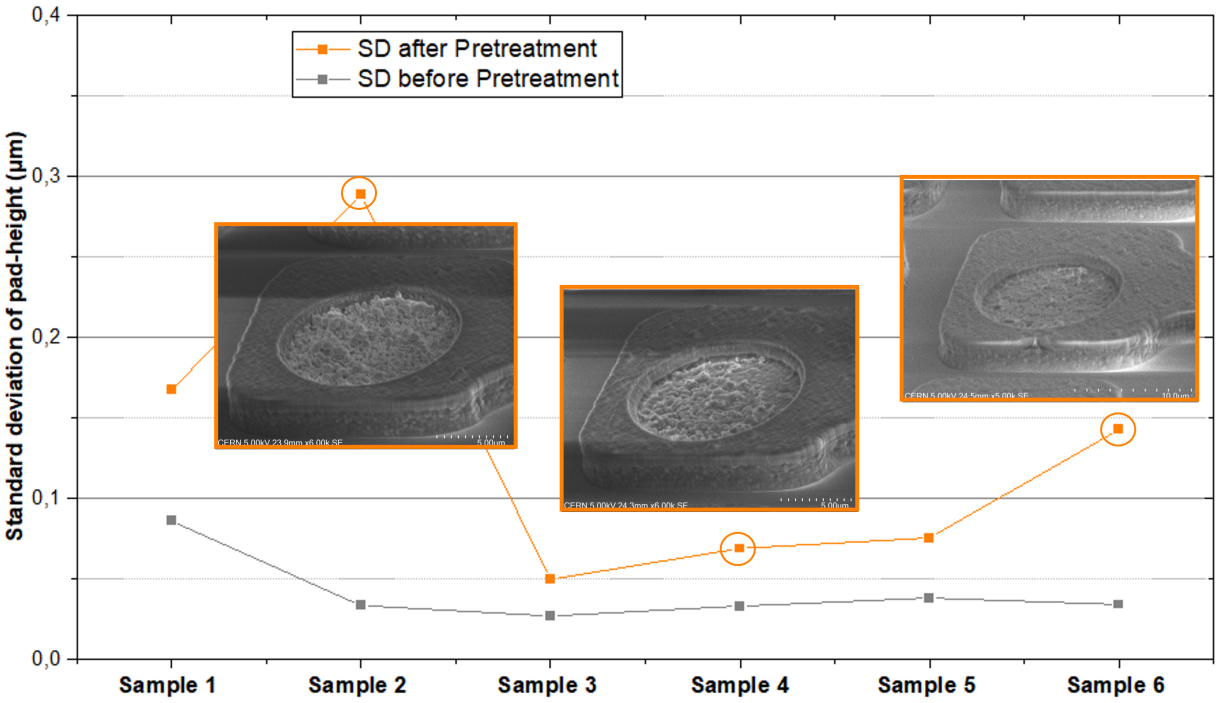


Figure 3.5: Measurements of the roughness of the pad of all six samples after pretreatment (orange) and before pretreatment (grey). The picture inlets show the corresponding SEM images of samples 2, 4 and 6 after the respective pretreatment steps.

All six samples were subsequently treated in the same beaker using the same ENIG processing steps. Nickel deposition was carried out for 10 minutes at 85 °C. The immersion gold step was then carried out for five minutes at 80–85 °C. More detailed process information can be found in Table 3.2.
The six samples underwent different pretreatments, but all underwent the same ENIG process. Assuming the ENIG process has an identical effect on all samples, any differences observed after ENIG can be attributed to differences in pretreatment. With this in consideration, the samples were reanalysed using SEM and EDS after the ENIG process.

Table 3.2: ENIG steps, Make-up solutions and parameters

No.	Process	Make-up	Parameter
1	Rinsing	100% water*	< 1 min
2	Nickel deposition	20% NI Make-up HP, 10% NI Solution HP, 70% water*	10 min, 85°C
3	Rinsing the sample	100% water*	< 1 min
4	Immersion gold	75% SMT Make up, 25% water*, 2 g/l SMT Gold Salt	5 min, 80-88°C
5	Rinsing the sample	100% water*	< 1 min

water* = de-ionized water; the percentages (%) are shown by volume.

Figure 3.6 shows an SEM image of Sample 6 after ENIG treatment, alongside the corresponding EDS analysis. The SEM image reveals that the passivation opening has been filled up. The EDS analysis clearly identifies the materials as nickel, phosphorus and gold. Aluminium is shown in red and silicon in light blue. Nickel is shown in green, phosphorus in yellow, and gold in orange. During nickel deposition, nickel and phosphorus are deposited on the pad. The immersion gold step then applies a thin layer of gold. Nickel, phosphorus and gold were detected in all six samples after ENIG. Since nickel and phosphorus only deposit on zinc, it is assumed that a small amount of zinc (below the EDS detection limit) was present on all pads after pretreatment, also on the samples without dedicated zincation steps or after zinc removal steps.

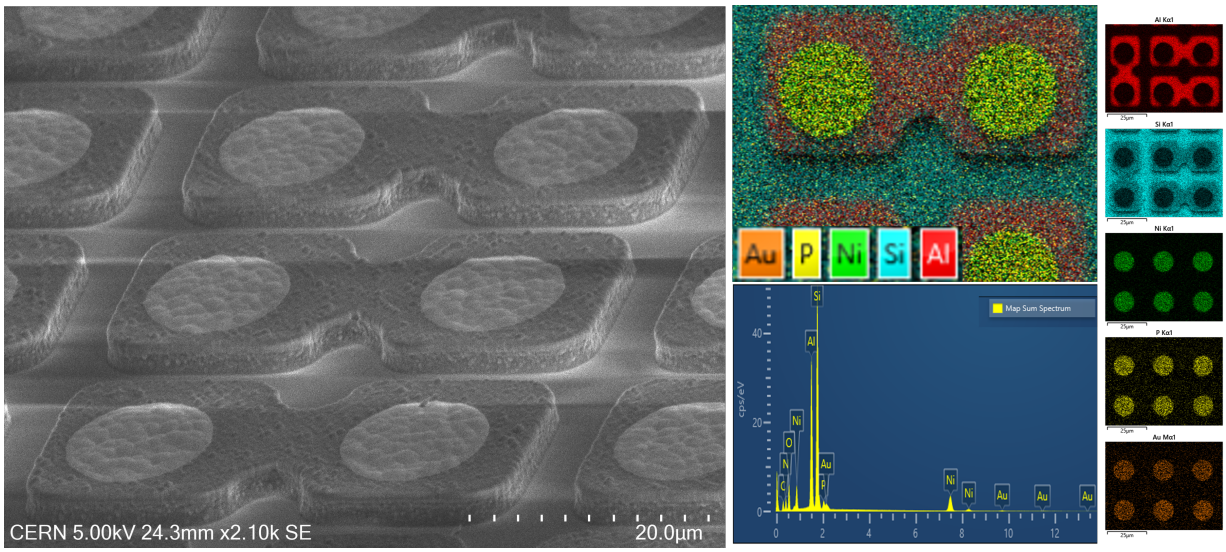
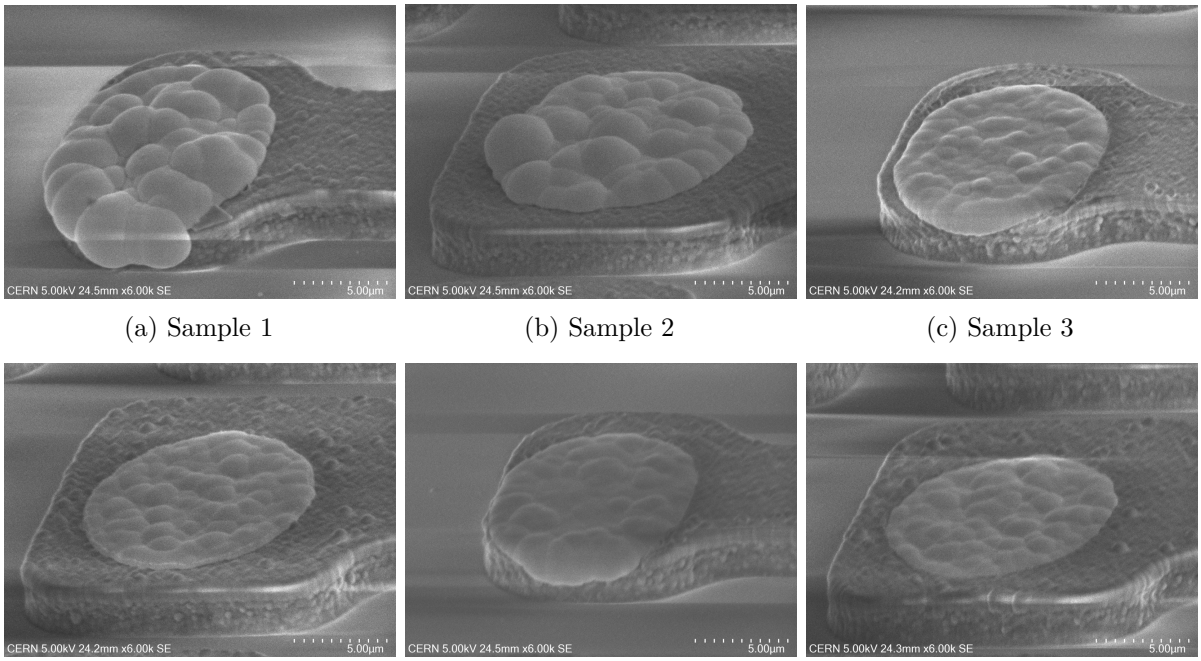


Figure 3.6: SEM image of Sample 6 after ENIG and corresponding EDS analysis.

Figure 3.7 shows SEM images of all six samples after ENIG processing. The passivation opening in each sample is filled with nickel and phosphorus and coated with gold. However, the nickel bumps in the resulting images look significantly different between samples.
Samples 1 and 2 have very large nickel bumps consisting of several clearly recognisable individual spheres. This also makes the surface appear significantly rougher and more uneven. The shape of the nickel bumps is probably due to the shape of the zinc surface after pretreatment. Nickel growth begins simultaneously across the entire zinc surface. As the zinc surface was very inhomogeneous in samples 1 and 2, this also results in inhomogeneous nickel bumps. In figure 3.4a the zinc spheres can be seen hanging over the passivation after pretreatment, resulting in a corresponding nickel bump that also extends beyond the passivation opening in figure 3.7a.
Samples 3–6 all look similar. Once again, the passivation opening has been filled with nickel bumps. However, the bumps stop at approximately the same height as the passivation layer. Small spheres can also be seen here. Compared to samples 1 and 2, these spheres have a smaller diameter, resulting in less roughness of the nickel bumps.



(a) Sample 1 (b) Sample 2 (c) Sample 3

(d) Sample 4 (e) Sample 5 (f) Sample 6

Figure 3.7: SEM images of samples 1-6 after their respective pretreatment followed by ENIG deposition with the same parameters used for all samples.

The roughness of the six samples was then measured again. Figure 3.8 shows the results for the standard deviation of the height values. The measurements for the samples after ENIG are shown in green, the measurements for the samples after pretreatment in orange and the measurements for the aluminium before treatment in grey.

As can be seen, the roughness increases as a result of the ENIG treatment. This increase is more significant than that observed after pretreatment. However, it is noticeable that not all samples increase to the same extent. Sample 1 has the most uneven surface, with a standard deviation of 0.9 µm. Sample 2 has a standard deviation of just under 0.5 µm, which is significantly lower. The standard deviation then drops again to approximately 0.4 µm for sample 4, and to just over 0.3 µm for sample 6, which has the lowest standard deviation. This trend is also visible in the SEM images. The difference between samples 1 and 2 and the others is clearly visible.
These results show that multiple zincation steps in the pretreatment lead to a more homogeneous zinc layer on the pad. The subsequent ENIG process starts on the zinc layer created in the pretreatment. The more homogeneous zinc layer also makes the nickel bump more homogeneous.

To confirm the results, AFM measurements were taken of samples 2, 4 and 6. These can be seen in Figure 3.9. The measured area of the samples was 10x10μm on the bonding pads of the samples. Both the 2D and 3D representations of the three samples are shown. The AFM measures the surface structure very accurately. Small spheres can be seen in all images. These spheres were already visible in the SEM images from Figure 3.7. Sample 2 had one zincation in the pretreatment, sample 4 had two zincations in the pretreatment and sample 6 had three zincations in the pretreatment. This leads to spheres of different sizes in the nickel deposition. Both the height and diameter of the spheres decrease from sample 2 to sample 4 to sample 6.

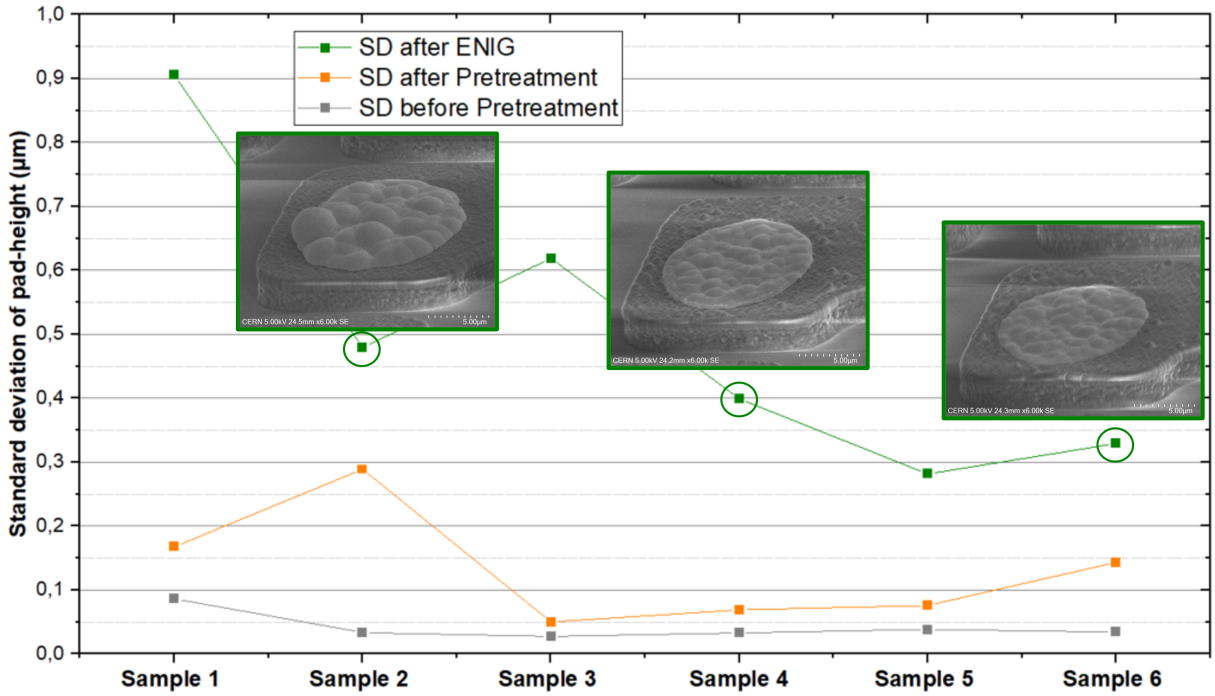
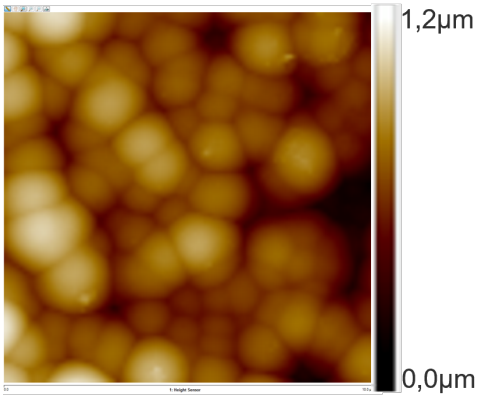
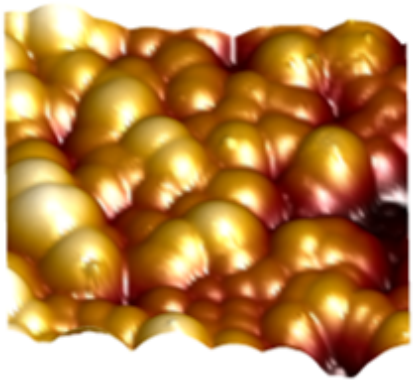


Figure 3.8: Measurements of the roughness of the pad of all six samples after ENIG (green), after pretreatment (orange) and before pretreatment (grey). The picture inlets show the corresponding SEM images of samples 2, 4 and 6 after ENIG.

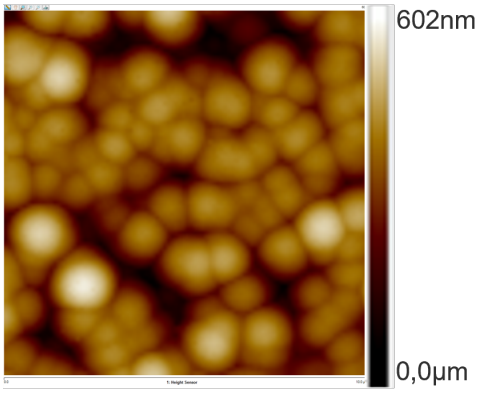
Due to the finer zinc structure, the nickel deposition starts more uniformly. As a result, the growing spheres join together more quickly, leading to a more homogeneous surface. The AFM measurements confirm the results shown above.
Since the most homogeneous surface possible is desired for the nickel bump, the ENIG process can be improved by multiple zincation steps.



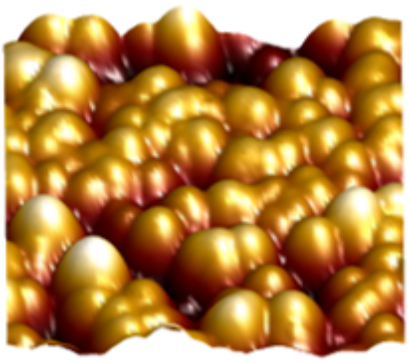
(a) Sample 2



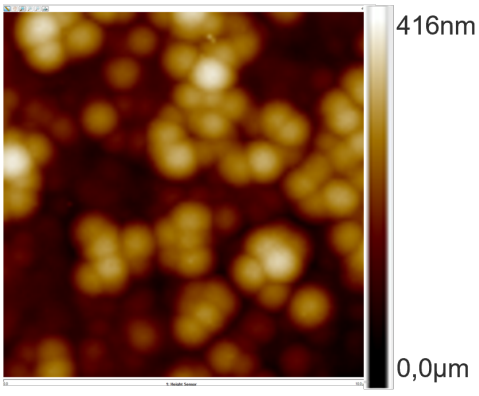
(b) Sample 2 - 3D visualisation



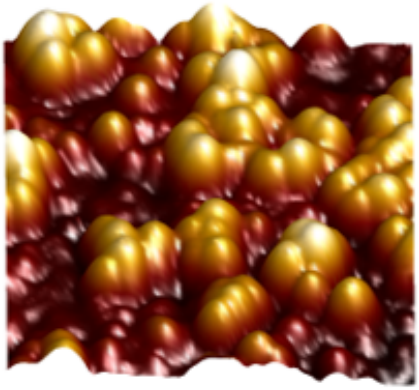
(c) Sample 4



(d) Sample 4 - 3D visualisation



(e) Sample 6



(f) Sample 6 - 3D visualisation

Figure 3.9: AFM measurements of samples 2, 4 and 6 after ENIG on a 10μmx10μm square area on the bonding pads, in top view with height scale (a, c and e) and in 3D visualisation (b, d and f).

3.2 Influence of nickel deposition

The aim of this section is to determine the effect of individual parameters during nickel deposition. The influence on the deposition rate and the uniformity was investigated.

3.2.1 Nickel deposition reference

In order to determine the effects of the parameters, a reference must first be created. For this purpose, a test was carried out using the starting parameters recommended by the manufacturer of the chemicals.

Processing

Five samples were pretreated using the pretreatment recipe from Table 3.1 with three zincations. These samples were plated in the same nickel solution for different durations. The contents of the nickel solution are shown in Table 3.3 and are the same for all subsequent tests unless explicitly stated otherwise.

Table 3.3: Make-up solution for nickel deposition

No.	Substance used	Amount
1	De-ionized water	350ml
2	Xenolyte Nickel Make-up HP	100ml
3	Xenolyte Nickel Solution HP	50ml
4	Xenolyte Nickel Stabilzer C	0,1ml
5	Ammonia acid 24,5%	~10ml depending on the desired pH

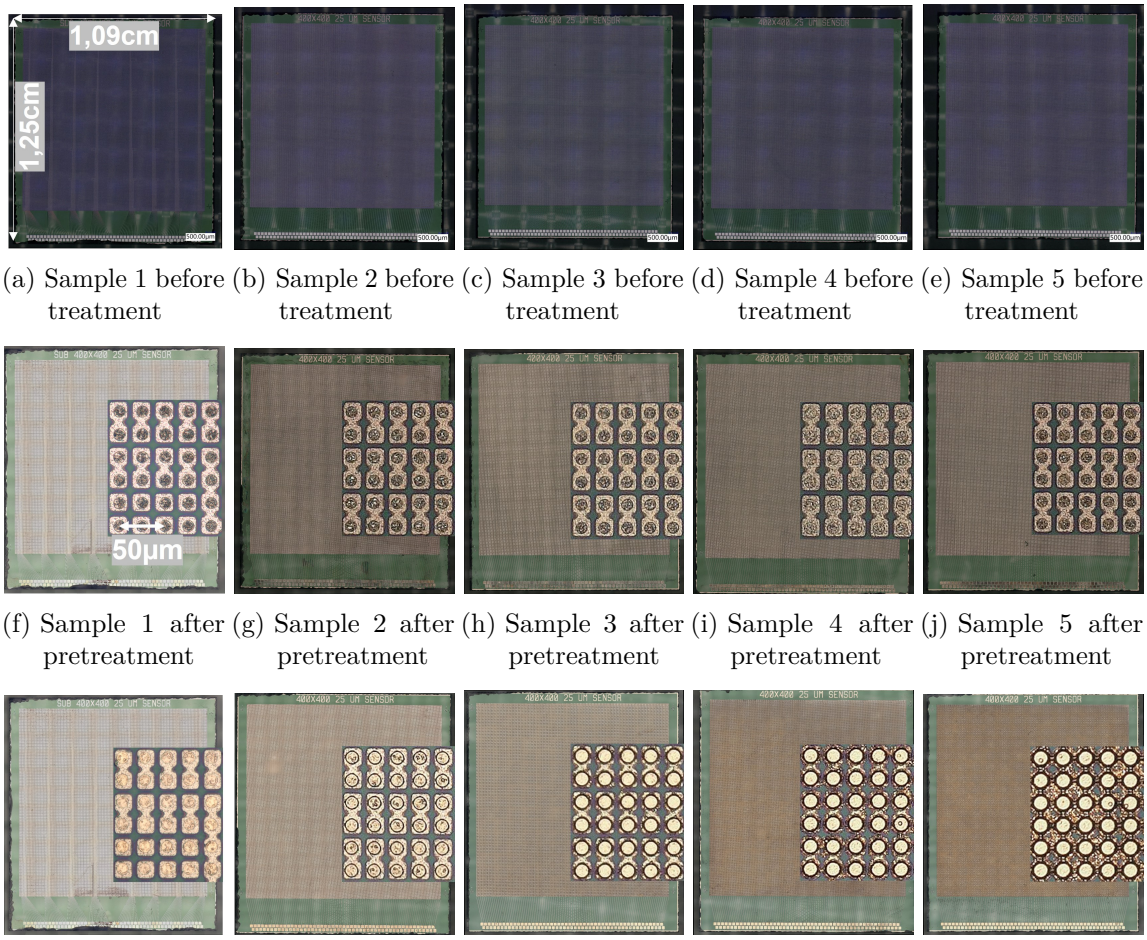
The chemical manufacturer recommends the following starting values for the nickel deposition: a solution temperature of 85°C, a pH value of 4.8, and a stabiliser concentration of 200 µl/l. This should result in a deposition rate of 6–9 μm/h.
The five samples were plated in the nickel solution for 10, 20, 30, 40 or 50 minutes. They were then treated in an immersion gold bath at approximately 80–88 °C for 5 minutes. The ingredients for the gold bath can be found in Table 3.4; the gold bath is operated in a large tank which is kept for several months and adapted in irregular intervals. However, since the resulting gold layer is only a few tens of nanometres thick, any differences for the obtained height of the nickel bumps due to differences in the gold bath are negligible.

Table 3.4: Make-up solution for immersion gold

No.	Substance used	Amount
1	De-ionized water	25%vol
2	Aurolectroless SMT Make-up Solution	75%vol
3	Aurolectroless SMT Gold Salt	2g/l

Microscopic investigation and analysis of results

Figure 3.10 shows light microscope images of the five samples at three stages: before treatment, after pretreatment, and after nickel and gold exposure. All the chips have the same dimensions (1.25 cm x 1.09 cm) and pitch (25 μm). After pretreatment, black discolouration is visible on the pixel pads. This is the deposited zinc, which is visible on all five samples.
The longer the chips were plated, the more 'golden' they appear in the images 3.10k-3.10o. Additionally, the radius of the ENIG bumps increases with longer plating times. Smaller gold dots can also be seen between the pixels with longer plating times.



(a) Sample 1 before treatment (b) Sample 2 before treatment (c) Sample 3 before treatment (d) Sample 4 before treatment (e) Sample 5 before treatment

(f) Sample 1 after pretreatment (g) Sample 2 after pretreatment (h) Sample 3 after pretreatment (i) Sample 4 after pretreatment (j) Sample 5 after pretreatment

(k) Sample 1 after 10min ENIG (l) Sample 2 after 20min ENIG (m) Sample 3 after 30min ENIG (n) Sample 4 after 40min ENIG (o) Sample 5 after 50min ENIG

Figure 3.10: Light microscope images of the five samples: before treatment (a–e); after pretreatment with three zincations (f–j); and after the ENIG process for 10, 20, 30, 40 or 50 minutes (k–o). Images of the samples after pretreatment and after the ENIG process also include a zoomed-in view showing individual pixels.

In order to obtain images with a better resolution of the ENIG bumps, images of individual pixels were taken with a SEM. In addition, the median height and standard deviation of the bump

height were determined using the software described in section 2.5. The results are shown in Figure 3.11. The time in the nickel solution is shown on the x-axis, the median height on the y-axis, and the standard deviation of the height as error bars. In addition, corresponding SEM images are connected with arrows.

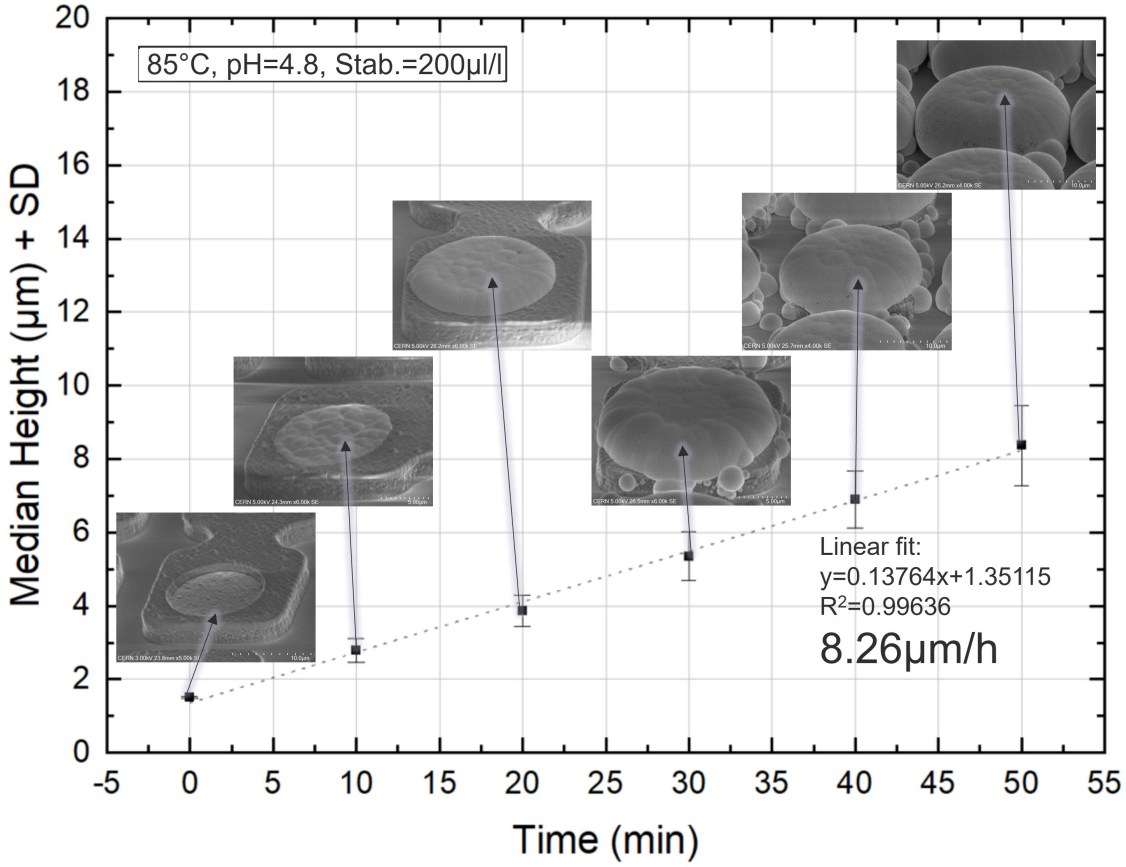


Figure 3.11: Height measurements and SEM images of the plating series under standard conditions (85°C, pH = 4.8, 200 μl/l stabiliser) with different deposition times for the five samples.

The SEM image in the bottom left of Figure 3.11 shows a pixel before treatment. The height difference between the aluminium and the lower passivation surfaces next to the pixels was determined as 1.5 μm. The remaining SEM images show pixels after the respective ENIG process. Sample 1, which was plated for 10 minutes, has a height difference of approximately 3 μm from the ENIG bump surface to the passivation surface between the pixels, and the passivation opening is completely filled with ENIG.
The ENIG bump grows as the plating time increases. A linear fit was applied to the height measurements. The R^2 value is over 0.99, indicating a good linear fit. Accordingly, the rate at which nickel is deposited remains constant. The slope of the linear fit can be used to calculate the nickel deposition rate. For the measured samples, the parameters 85°C, pH=4.8 and a stabiliser concentration of 200 μl/l result in a deposition rate of 8.3 μm/h. Therefore the determined deposition rate falls within the range specified by the chemical supplier (6–9 μm/h).

Parasitic ENIG growth

The SEM images show that small spheres appear at the edge of the pad after 30 minutes. These spheres also appear to grow larger as the plating time increases. Eventually, they merge with the main nickel bump. These spheres are not visible before 30 minutes. One possible explanation for this parasitic ENIG growth are pinholes in the passivation of the chips [34, 35]. This allows nickel to grow from the aluminium through the pinhole which can arise during production due to stress in the silicon nitride layer [34]. The nickel only reaches the opening of the pinhole after a certain plating height has been achieved. From this point onwards, it can grow in all directions resulting in spheres. The different sizes of the spheres are explained by the varying lengths of the grown paths through the pinhole.

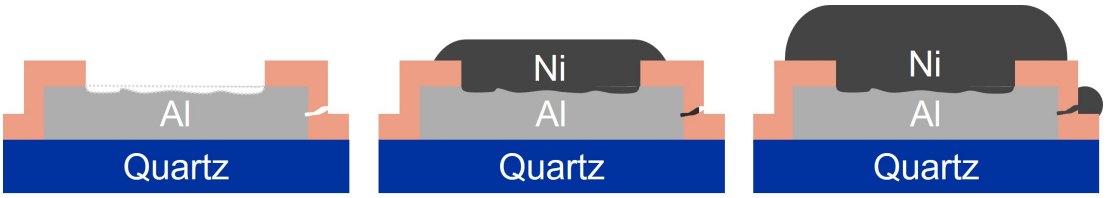


Figure 3.12: Schematic representation of nickel growth through a pinhole over time.

Figure 3.12 illustrates the pinhole effect schematically. The image on the left shows a pixel before nickel deposition. The pinhole is shown schematically on the right-hand edge. In the middle image, the nickel is growing. Once it has grown over the passivation opening, the nickel bump takes on its characteristic rounded edges. The nickel growing through the pinhole has not yet reached the surface. In the image on the right, the nickel bump has grown further. It has also grown through the pinhole, creating a sphere through isotropic growth.
In an attempt to confirm this hypothesis, efforts were made to detect the pinholes using FIB, ideally revealing nickel growth through a pinhole. To achieve this, layers were removed step by step with a FIB, and SEM images were taken if a pinhole became visible. Figure 3.14 shows the region that was examined. The direction in which material was removed is illustrated on the right picture in blue. Careful removal of material was carried out at positions 1 (P1) and 2 (P2) to detect any pinholes that might be present.

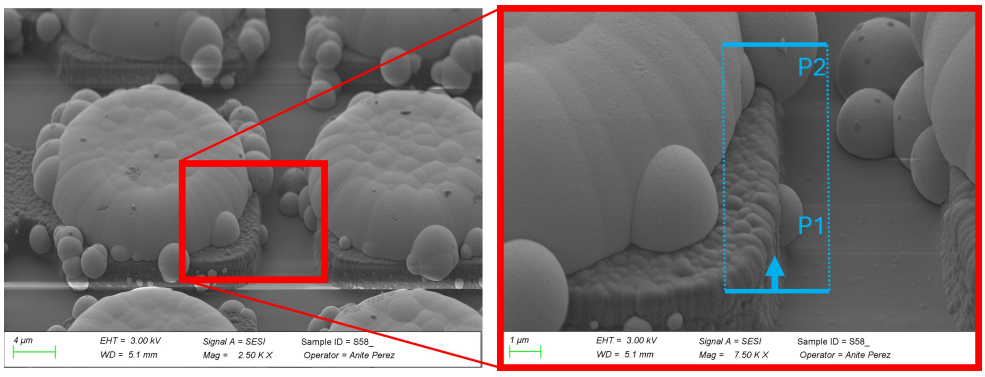


Figure 3.13: SEM images of the position where the sample was examined for pinholes, as well as the direction in which the material was removed using the FIB.

Figures 3.14a and 3.14b show cross-sections of position 1, while figures 3.14c and 3.14d show cross-sections of position 2. The aluminium pad can be seen on the left-hand side of all images. It is covered by the passivation layer. Small ENIG spheres are visible on the edge of the passivation layer. Red arrows mark areas that show pinholes. As these pinholes are very small and may have a winding path, they are difficult to capture completely in a two-dimensional image. However, the images indicate that some pinholes go through the entire passivation layer. No nickel growth took place through these pinholes as they do not end in the centre of a sphere. The reason for this could be that those pinholes are either too small or not continuous. Nevertheless, the images prove the presence of pinholes in the passivation. Furthermore, image 3.14a reveals that the passivation on the aluminium pad's edge is notably thinner, raising the probability of pinholes penetrating the passivation.

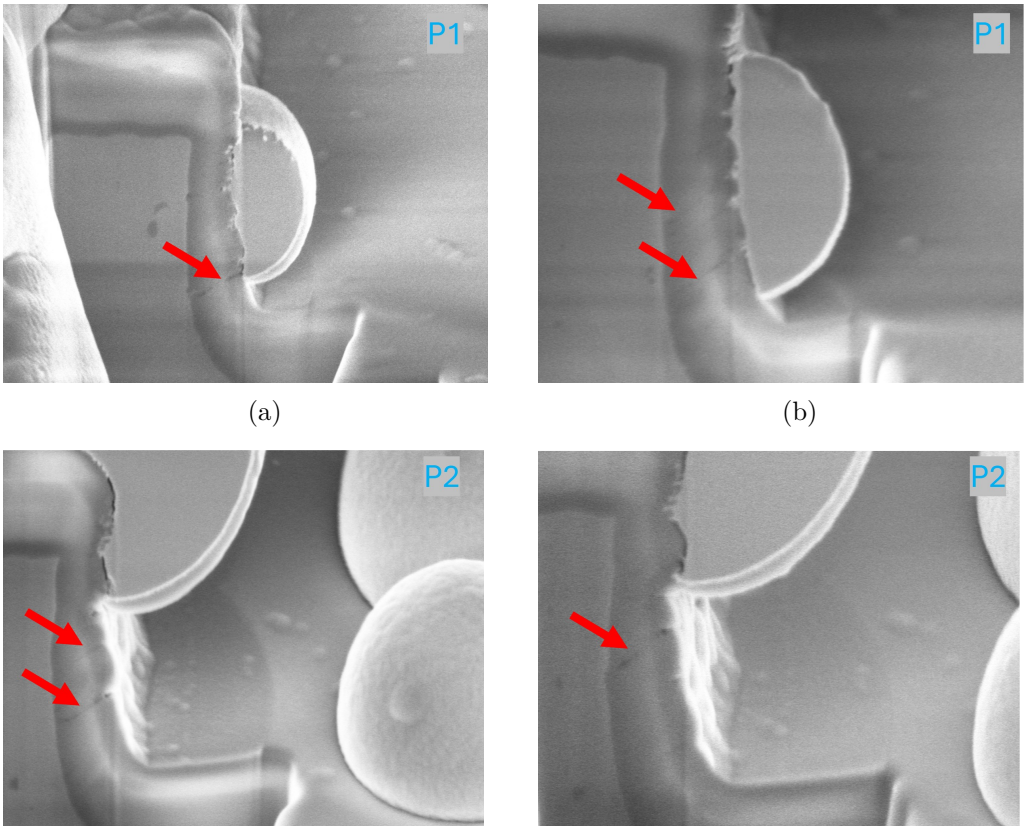
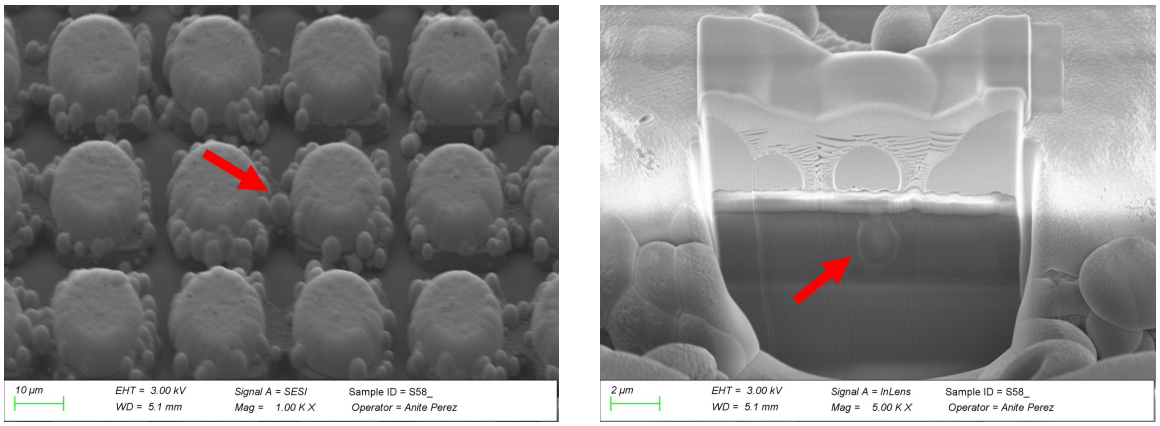


Figure 3.14: SEM images after FIB cross-section showing the pinholes in the passivation. Figures a and b show cross-sections taken at position 1, while figures c and d show cross-sections taken at position 2.

FIB cross-sections were performed at a different position, shown by the red arrow in Figure 3.15. There, a relatively large ENIG sphere has grown between the ENIG bumps. The area was coated with a thin layer of platinum to enable clearer images to be taken. Figure 3.15b shows the area after the FIB cross-section. The ENIG bumps can be seen on the left and right. The platinum layer that was applied can be seen at the top of the image. Beneath the platinum layer are the

edges of the ENIG bumps, with the ENIG sphere to be examined in the middle. Below that are the passivation layer, the aluminium pad and the quartz layer. A bubble is visible under the ENIG sphere which is marked with a red arrow. This bubble is centrally located under the sphere. It is conceivable that there is a pinhole in front of or behind this two-dimensional image. During pretreatment, aluminium was slightly etched through the pinhole, causing the bubble to open. During zincation, zinc was deposited on the bubble's surface, and nickel was deposited during nickel deposition. Thus, the bubble was filled with nickel, which grew through the pinhole and created the sphere on the passivation surface. To confirm this assumption, more locations like this would need to be found and analysed using EDS.



(a) Examined position before cross-section.

(b) Examined position after cross-section.

Figure 3.15: FIB cross-section taken at a different position, examining an ENIG sphere between two ENIG bumps.

3.2.2 Effect of temperature

To investigate the effect of temperature on nickel deposition, a series of tests was carried out on six samples similar to those in section 3.2. All samples underwent the same pre-treatment involving three zincations and were plated in identical nickel solutions. The only variable was the temperature of the nickel solution. For three of the samples, the hotplate temperature was set to 80 °C (instead of the nominal 85 °C) during deposition. The deposition times were 30, 40 and 50 minutes. For the other three samples, the temperature was set to 90 °C. The deposition times were 10, 20 and 30 minutes.
Subsequently, SEM images of individual pixels of the differently treated samples were taken and the median height and uniformity of the ENIG bumps were determined.
Figure 3.16 shows the results of the height measurements and the corresponding SEM images. The X-axis shows the time in the nickel solution and the Y-axis shows the median height of the ENIG bumps, with the standard deviation of the height values shown as error bars. The deposition series at 80°C is shown in blue and the deposition series at 90°C in red. For comparison, the deposition series at 85°C from section 3.2 is also shown. For both lower and higher temperatures, the measured values show a good linear fit, with R^2 values above 0.99. Deposition at a lower temperature of 80°C results in a lower deposition rate of 5.0 μm/h instead of 8.3 μm/h. A higher

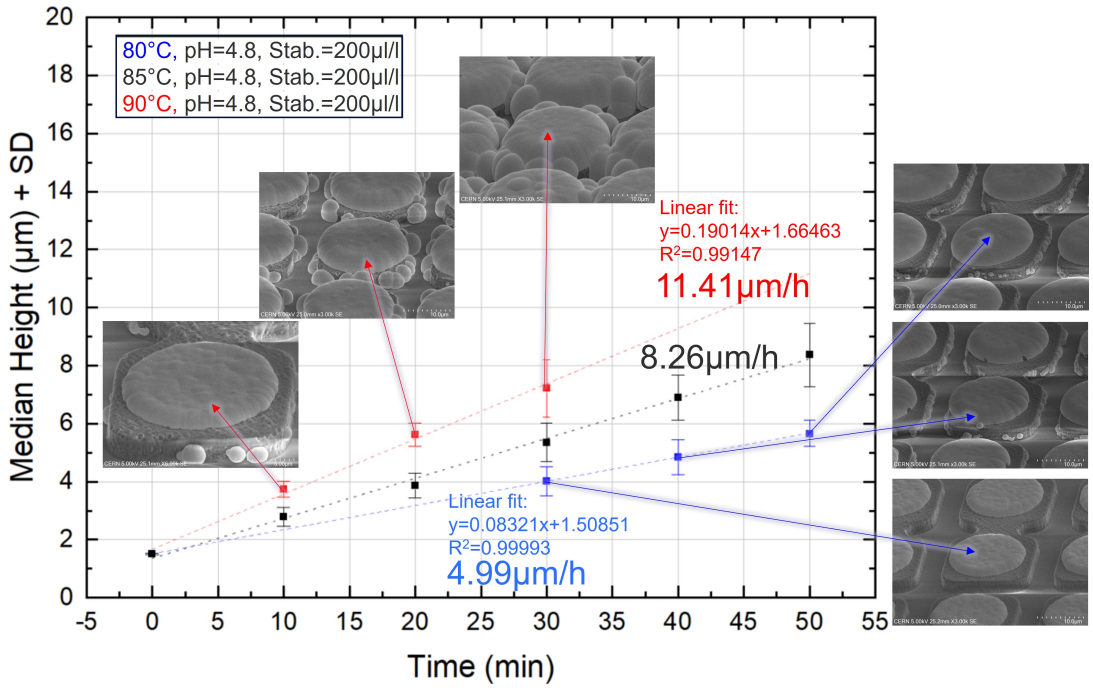


Figure 3.16: Plating series with reduced and increased temperatures during deposition and different deposition times.

temperature of 90°C results in an increased deposition rate of 11.4 μm/h. ENIG bumps merge after 50 minutes at a deposition temperature of 85°C. However, the lower deposition rate at 80°C results in bumps that are still not merged after 50 minutes. At an increased deposition rate at 90°C, the bumps have merged after just 30 minutes.
Changes in the deposition rate also influence the formation of spheres that grow through pinholes. For the lower deposition rate, spheres form later and are smaller. For the increased deposition rate, sphere from earlier and are bigger.

3.2.3 Effect of pH value

To investigate the effect of the pH value on nickel deposition, a series of tests was carried out on six samples similar to those in sections 3.2.1 and 3.2.2. All samples underwent the same pre-treatment involving three zincations, and were plated in identical nickel solutions. The only variable was the pH value of the nickel solution. Therefore, the amount of ammonia acid was varied to achieve a pH of 3.8 for the first three samples and 5.8 for the next three samples. The temperature was 85°C for all samples. The samples were treated for 20, 30, or 40 minutes.
Subsequently, SEM images of individual pixels of the differently treated samples were taken and the median height and uniformity of the ENIG bumps were determined. Figure 3.17 shows the results of the height measurements and the corresponding SEM images. For comparison, the deposition with pH 4.8 is shown again.
The linear fit for a reduced pH value of 3.8 is worse, with an R^2 value of 0.84. For an increased pH value, the ENIG bumps merge after 20 minutes. Therefore the programme from section 2.5

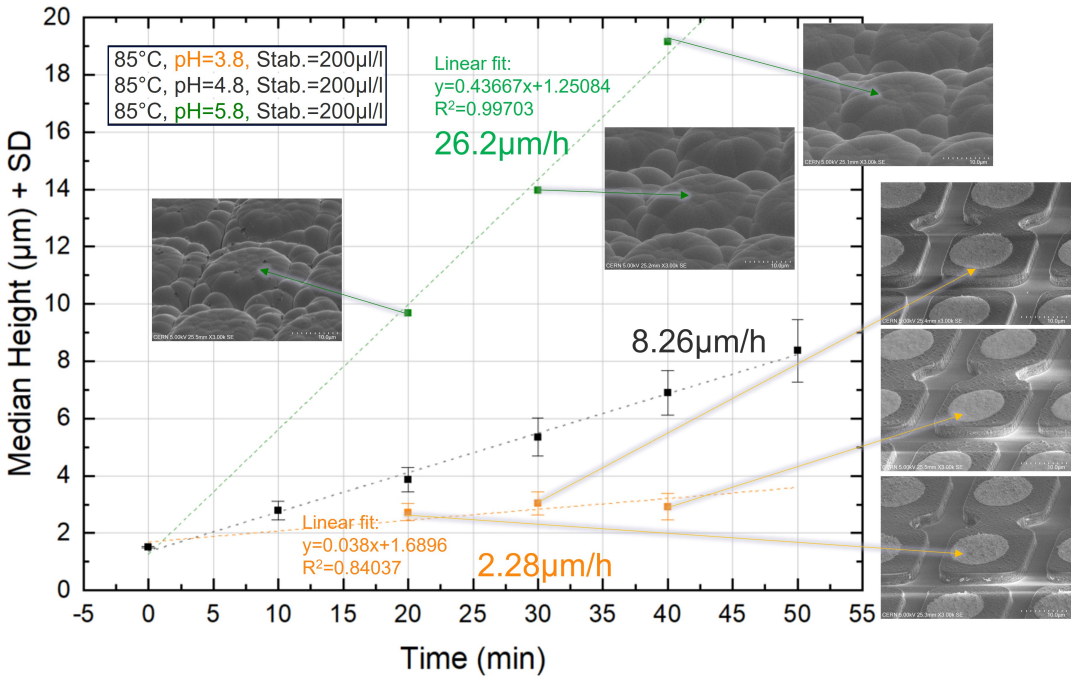


Figure 3.17: Plating series with reduced and increased pH value during deposition and different deposition times.

cannot be used to determine the height. Several manual measurements were taken from the edge of the matrix and averaged to determine the height. This resulted in an good linear fit, with an R^2 value of over 0.99.
A reduced pH value of 3.8 lowers the deposition rate to 2.3μm/h compared to 8.3μm/h. An increased pH value of 5.8 raises the deposition rate to 26.2μm/h compared to 8.3μm/h.

3.2.4 Effect of stabilizer concentration

To investigate the effect of the stabilizer concentration on nickel deposition, a series of tests was carried out on six samples similar to those in sections 3.2.1, 3.2.2 and 3.2.3. All samples underwent the same pre-treatment involving three zincations, and were plated in identical nickel solutions. The only variable was the stabilizer concentration in the nickel solution. Therefore, the amount of stabilizer was varied from the nominal 200 μl/l to 0 μl/l for the first three samples and to 400 μl/l for the next three samples. The temperature was 85°C for all samples and the pH 4.8. The samples were treated for 10, 20, 30, or 40 minutes.
Subsequently, SEM images of individual pixels of the differently treated samples were taken and the median height and uniformity of the ENIG bumps were determined. Figure 3.18 shows the results of the height measurements and the corresponding SEM images. For comparison, the deposition with the nominal stabiliser concentration of 200 μl/l is shown as well.
The measured height values show good linear fits, with R^2 values of over 0.99, for both a lower and an increased stabiliser concentration. The deposition rate is 11.9 μm/h for a lower stabiliser concentration of 0 μl/l and 9.9 μm/h for an increased stabiliser concentration of 400 μl/l.

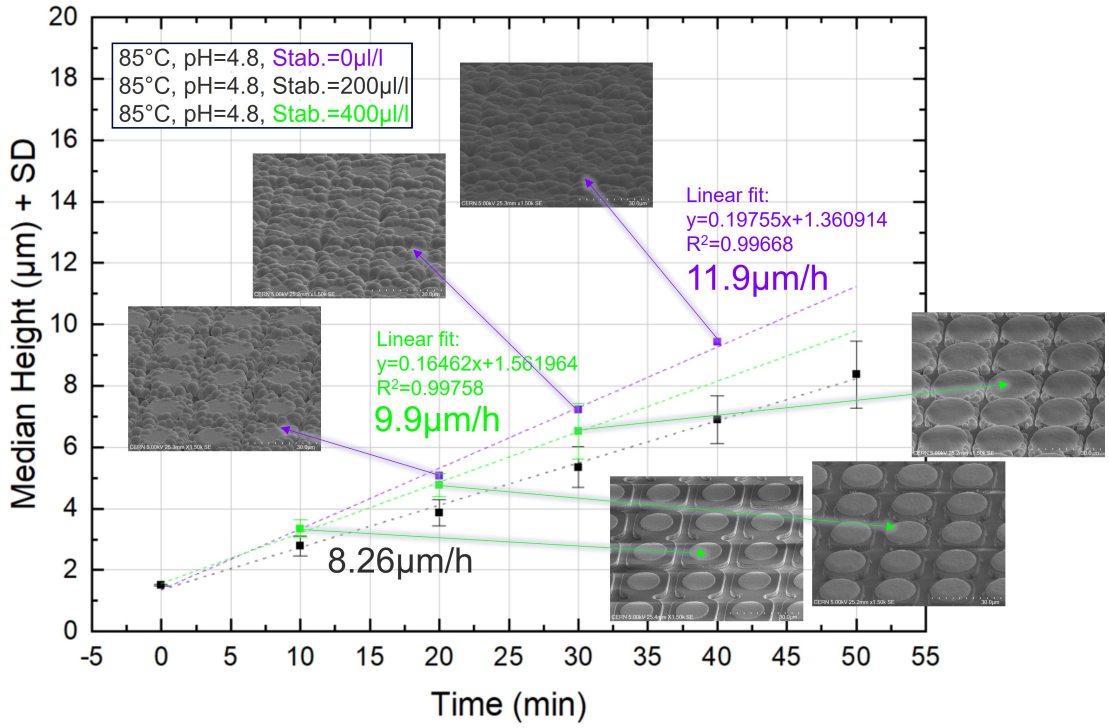
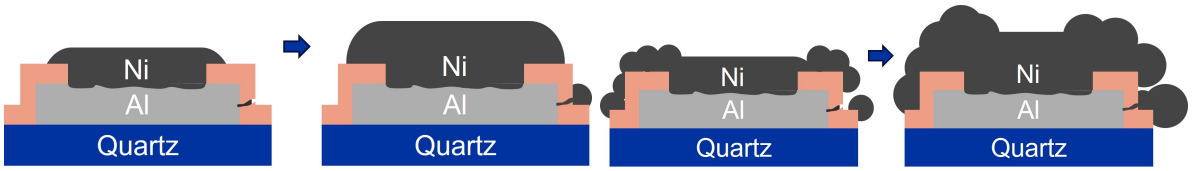


Figure 3.18: Plating series with reduced and increased stabiliser concentration during deposition and different deposition times.

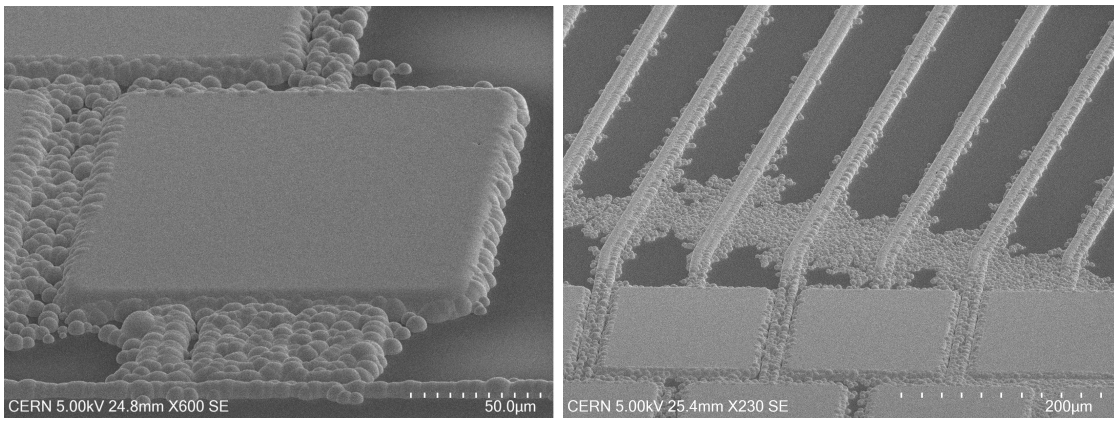
Changes in stabiliser concentration have less influence on the deposition rate than changes in temperature or pH value. However, the stabiliser concentration has a significant impact on the type of deposition. The spheres that form at the edge of the pads can be attributed to growth through pinholes. Due to growth through pinholes, however, the spheres must always be lower or equal to the height of the nickel bump. Figure 3.18 shows SEM images of samples with a stabiliser concentration of 0 µl/l. The spheres in these images are higher than the nickel bump. Therefore, these spheres cannot have been caused by growth through pinholes.



(a) Nickel growth through pinhole. (b) Nickel growth on passivation.

Figure 3.19: Schematic representation and comparison of nickel growth through pinholes and nickel growth starting on the passivation layer.

Without a stabiliser in the nickel solution, nickel deposition can start randomly on the passivation surface. Small spheres begin to grow on the passivation layer at the same time as the nickel bump, meaning they are always higher. Figure 3.19 illustrates this effect schematically.
Figure 3.20 shows SEM images of nickel deposition on the passivation between the contact pads and the connection lines.

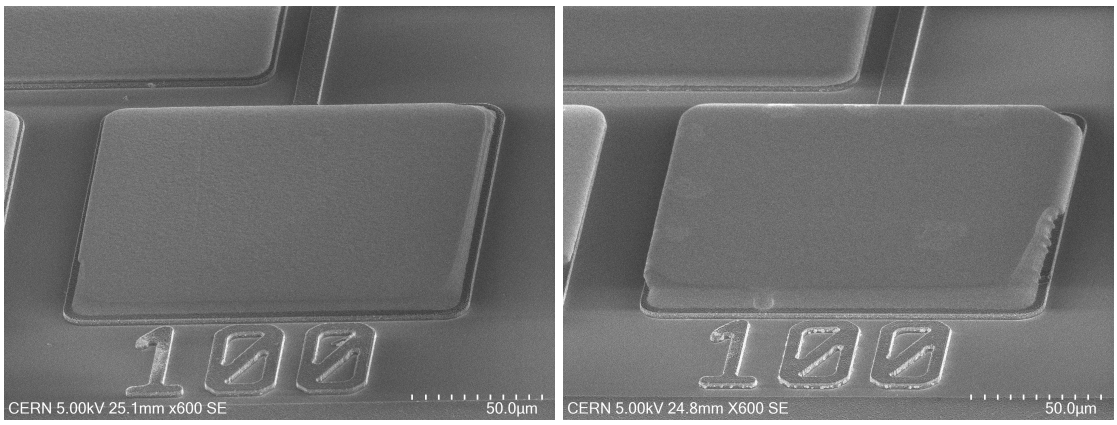


(a) Deposition begins on passivation between wire bonding pads.

(b) Deposition begins on passivation between connection lines.

Figure 3.20: SEM images showing nickel deposition on the passivation layer of samples with stabiliser concentration of 0μl/l.

The opposite effect can be seen with an increased stabiliser concentration of 400 μl/l. Figure 3.21 shows SEM images of wire bonding pads, where nickel deposition stops at the edge of the pad.
In conclusion, the stabiliser concentration should be neither too low, to prevent nickel deposition on the passivation layer, nor too high, to prevent a premature stop of the nickel deposition. For all subsequent plating, the stabiliser concentration is maintained at 200 μl/l.



(a) (b)

Figure 3.21: SEM images showing nickel deposition stopping at the edge of the contact pads in the periphery, for samples with a stabiliser concentration of 400 μl/l.

3.2.5 Effect of increased temperature and pH value

Section 3.2.2 showed that a higher temperature during nickel deposition results in a higher deposition rate. Section 3.2.3 showed that an increased pH value also results in a higher deposition rate. To investigate the possibility of combining these effects, a series of experiments involving two samples were conducted, with both the temperature and the pH value increased during nickel deposition. To prevent the pixels from merging, the following parameters were selected: a temperature of 90°C, a pH value of 5, and deposition times of 10 and 15 minutes. Both samples underwent the same pre-treatment involving three zincations, and were plated in identical nickel solutions. The stabiliser concentration was 200 μl/l.
Figure 3.22 shows the results of the height measurements and SEM images of the two samples. For comparison, the measurements from the series of 85°C/pH 4.8 and 90°C/pH 4.8 are also shown. The measured height values show a good linear fit, with a R^2 value of over 0.99. Therefore a deposition rate of 16 μm/h can be calculated. The deposition rate increases to 11.4 μm/h due to the increased temperature, and then rises again to 16 μm/h due to the slightly increased pH value. These measurements demonstrate that the effects of increased deposition rates due to higher temperatures or pH values can be superimposed.

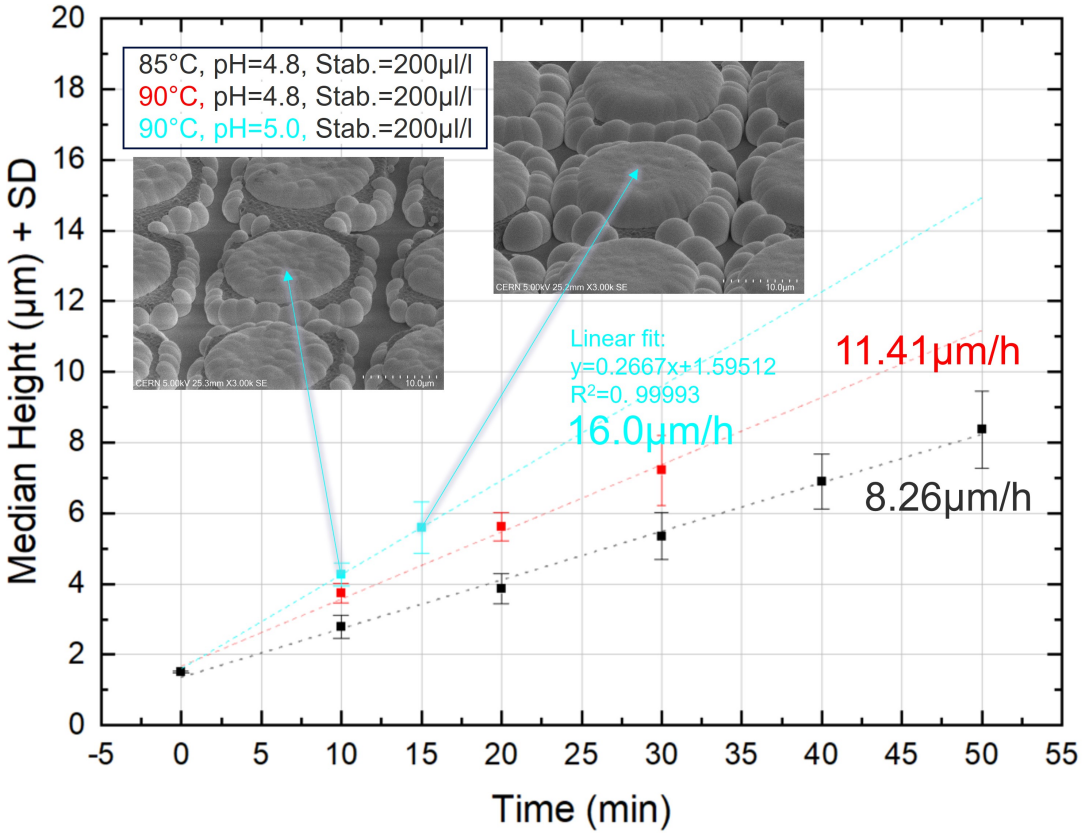


Figure 3.22: Plating series with increased temperature and pH value during deposition and different deposition times.

3.3 Discussion of plating results

Figure 3.23 shows the measured heights of the samples from the above sections, their linear fits, and the deposition rates derived from these. From the linearity of the fits, it can be concluded that changes in nickel concentration in the solution caused by plating and evaporation of the liquid have no significant effect on the speed of nickel deposition within this process setup. Consequently, the deposition rate remains consistent throughout one deposition series with specified parameters, resulting in good linear fits.

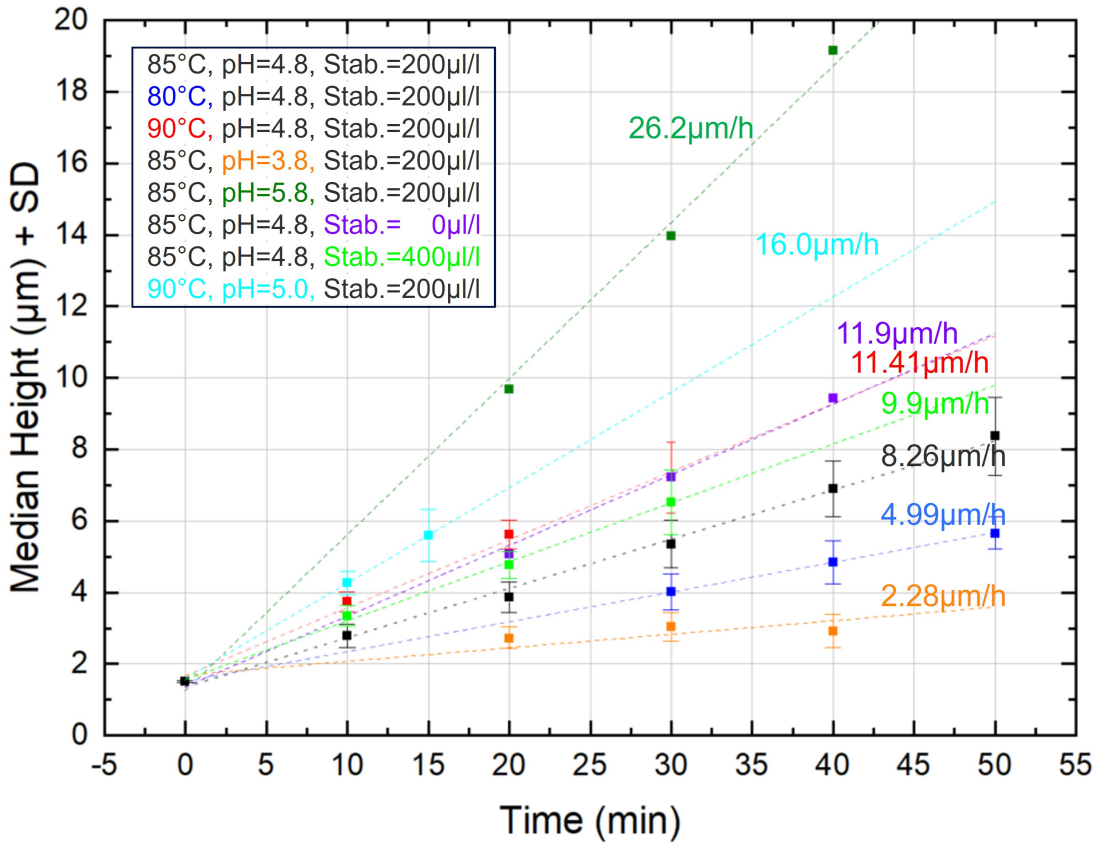


Figure 3.23: Plating series for all the above parameters.

The deposition rate and deposition type depend strongly on the temperature, pH value and stabiliser concentration parameters. Deposition rates ranging from 2.3 μm/h to 26.2 μm/h were achieved. This means that deposition rates outside the range specified by the chemical manufacturer (6–9 μm/h) are also achievable. The deposition rate depends mostly on the pH value and the temperature of the solution during deposition. Increasing the pH value from 4.8 to 5.8 has a greater effect (deposition rate +17.9 μm/h) than increasing the temperature from 85°C to 90°C (deposition rate +3.2 μm/h).
Besides the effect on the deposition rate, the effect on uniformity was also investigated. Therefore, the measured standard deviation of the height for the different samples were compared. The standard deviation has already been shown as error bars in the deposition rate graphs of the sections above. However, plotting them separately allows for a better comparison.

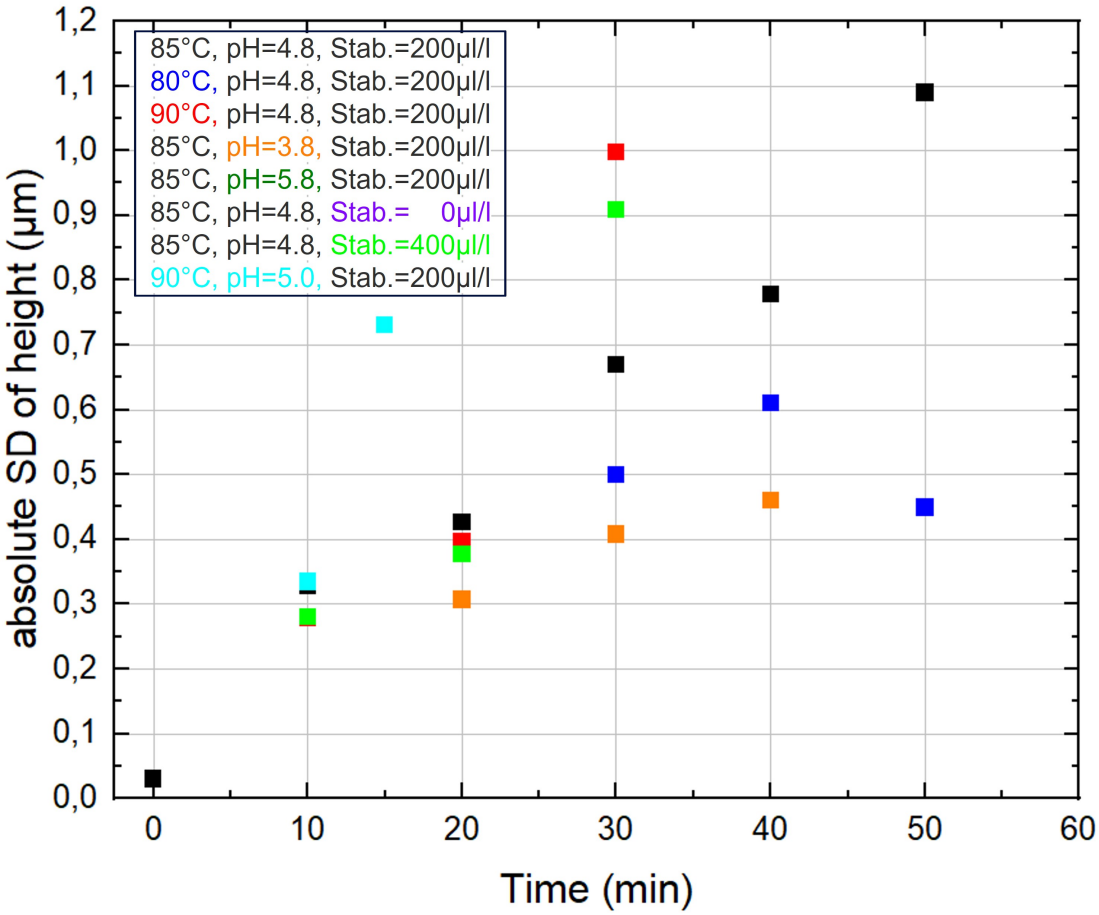


Figure 3.24: Absolute standard deviation of the height values of the samples that were plated with different parameters.

Figure 3.24 shows the absolute measured standard deviation for different samples over plating time. The standard deviation is very low without treatment, at less than 0.1 µm after 0 minutes of plating time, demonstrating a good uniformity of the aluminium pads. The other points show the standard deviation after ENIG plating with various parameters and plating times. As plating time increases, the standard deviation of the samples increases too. Samples plated using the starting parameters recommended by the chemical manufacturer (black dots) show an approximately linear increase in standard deviation over time. For samples with a higher deposition rate (red, light blue and green dots), the absolute standard deviation behaves similarly for short plating times. Subsequently, the absolute standard deviation for these samples increases more rapidly. The opposite is observed for samples with a lower deposition rate (dark blue and orange dots). These samples also exhibit a similar trend for short plating times, but subsequently have a lower absolute standard deviation for longer deposition times.

The effect of an increasing absolute standard deviation over time can also be linked to the ENIG height, as this increases over time too. To verify this, the absolute standard deviation was normalised to the height of the ENIG bump for each sample shown in Figure 3.25, resulting in

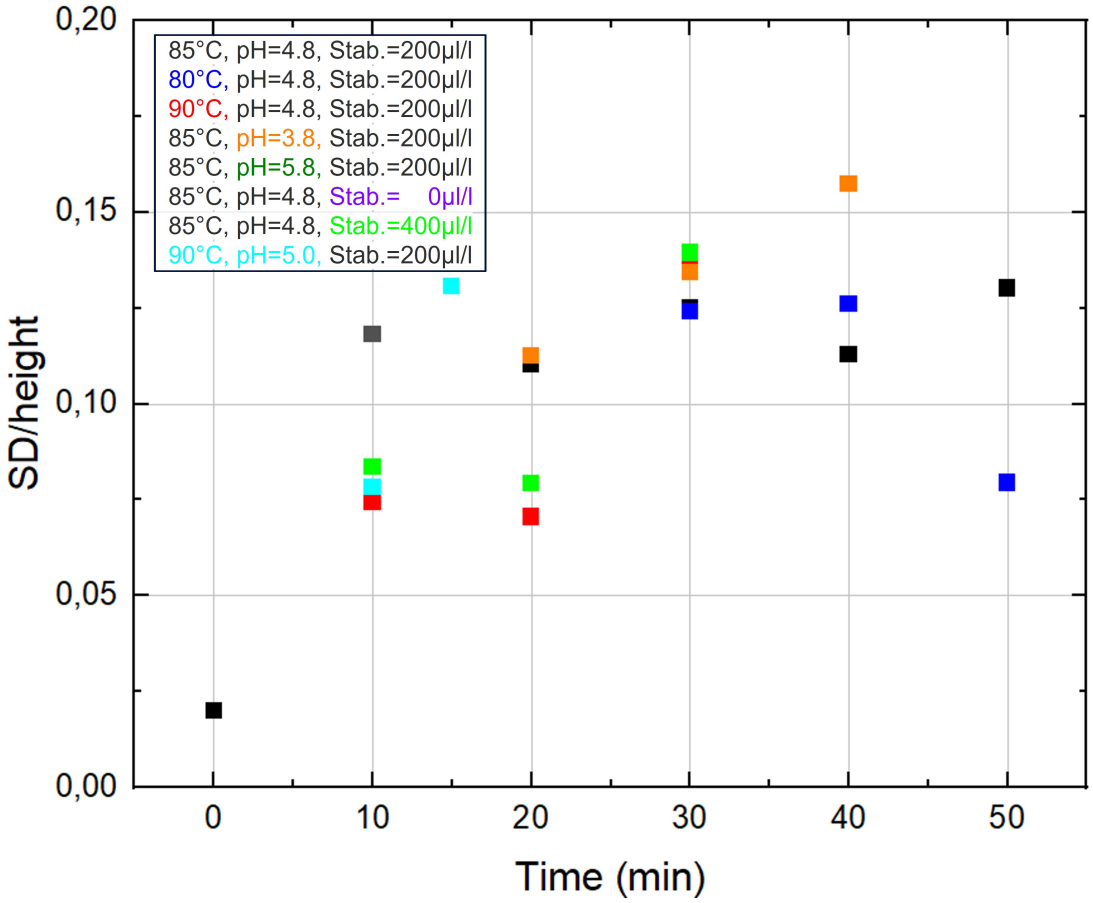


Figure 3.25: Relative standard deviation of the height values of the samples that were plated with different parameters.

a measure that expresses the standard deviation as a percentage of the bump's height. If the standard deviation were linked exclusively to the height of the ENIG bump, a horizontal line would be expected at a certain percentage. This appears to be the case at around 13 percent. However, it is noticeable that samples with higher deposition rates (red, light blue and green) have a lower relative standard deviation of around 7–8 percent, especially with short plating times. To conclude that an increased deposition rate leads to a lower relative standard deviation, a greater number of samples would need to be examined.

3.4 Hybridisation of plated samples

The following section examines the potential of ENIG plating for hybridisation with ACA. For this purpose, five 'SUB 400x400 25UM Sensor' and five 'SUB 400x400 25UM ASIC' chips, as described in Section 2.1, were plated. In the following hybridisation process, the samples are connected by thermo-compression using a flip-chip machine and ACF.

3.4.1 Plating

The ACF volume must be contained between the ENIG bumps. As the available volume between the chips depends on the ENIG bump height, a simulation-based optimisation was performed to determine the optimal bump height [3]. The optimisation resulted in a bump height of just over 4 µm for these chips and the used ACF material with 9 µm film thickness. In order to achieve this bump height, the chips were pretreated with three zincations. Subsequently, nickel deposition was carried out at a temperature of 90°C, a pH value of 5 and a stabiliser concentration of 200 µl/l for 10 minutes. The immersion gold process was carried out for 5 minutes at 85°C.
Subsequently, the achieved median bump height for all chips was determined to be approximately 4.2 µm, with a standard deviation of 0.3–0.4 µm depending on the chip. Figure 3.26 shows light microscope images of the ten samples after the ENIG process.

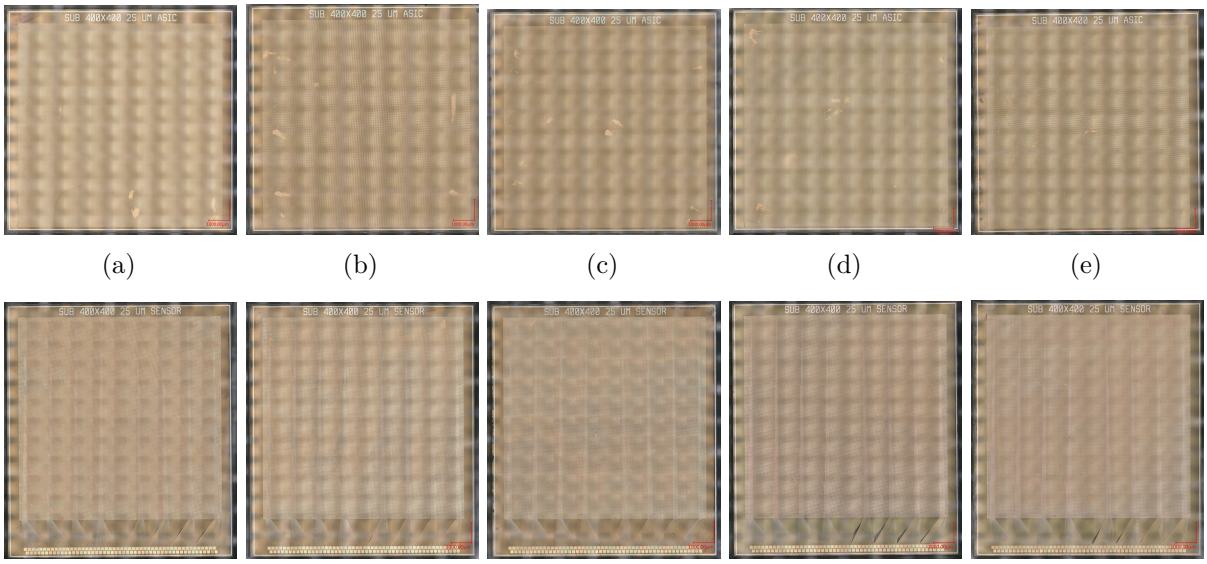
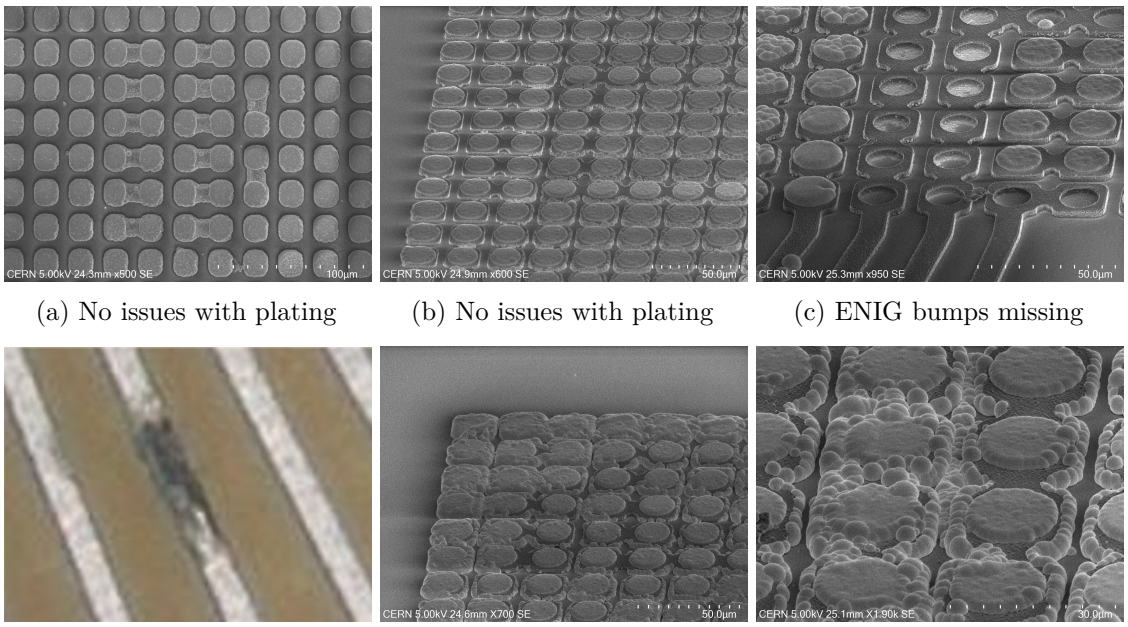


Figure 3.26: Light microscope images of the five 'SUB 400x400 25UM ASIC' in (a)-(e) and the five 'SUB 400x400 25UM Sensor' in (f)-(j) after the ENIG process.

Prior to hybridisation, all 480 islands on the ten samples were examined in detail as well as the connection lines on the 'SUB 400x400 25UM Sensor' chips. Figure 3.27 illustrates the various observed conditions and how they are categorised.
Figures 3.27a and 3.27b demonstrate the successful application of ENIG plating to both the ASIC and the sensor chip. This is the desired outcome, which is the case for 449 out of the 480 observed islands.
All other observations are undesirable effects that will impact the success of hybridisation. Figure 3.27c shows a small area where no ENIG bumps have formed. This occurred on one of the ten chips, in one of the corners, affecting two islands. For an island to be functional, a conductive particle must be trapped between the ENIG bumps in all 28 connections, creating a conductive contact. Without ENIG bumps, this is not possible, which inevitably leads to a non-functional island.

Figure 3.27d shows a cut connection line. If the aluminium line connecting the islands to the contact pads is cut, no current can flow and the island inevitably becomes non-functional.



(a) No issues with plating (b) No issues with plating (c) ENIG bumps missing

(d) Connection line cut (e) Some shorted pixel (f) Connection lines shorted

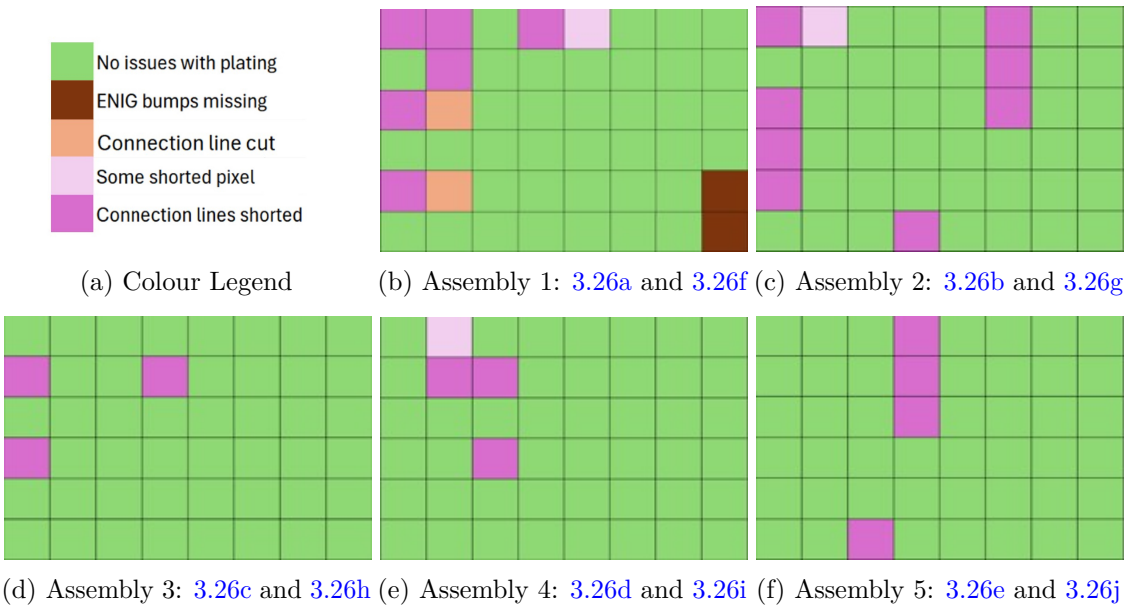
Figure 3.27: The categories into which the examined islands and connection lines were sorted, along with example images of each category.

Figure 3.27e shows shorted pixels within an island. The ENIG bumps have merged. This could be caused by passivation problems or by local concentration or temperature fluctuations during the ENIG process. If the pixels on an island are shorted, it is no longer possible to draw conclusions about the hybridisation connection, since the pixels will always be connected.
Figure 3.27f shows shorted connection lines. Due to the design of the test chips, the connection lines of the islands run next to each other. If a short occurs somewhere along the connection lines on the way to the island, it is impossible to make a statement about the connection within the island. In this case, there is always a connection between the two contact pads.
The above observations affect an island's functionality and must therefore be considered when interpreting the measurement results. A cut line inevitably results in a non-functional island in the measurement. However, hybridisation may still have occurred in the island. A shorted connection line will inevitably lead to a functional island in the measurement. However, the island may not actually have been connected by hybridisation.

3.4.2 Hybridisation

Chips (a) and (f), (b) and (g), (c) and (h), (d) and (i), and (e) and (j) from Figure 3.26 were hybridised to assemblies 1-5. Figure 3.28 shows the schematic arrangement of the islands within their respective assemblies. Each box corresponds to an island and its 28 connections. The results of the detailed examination of all the islands prior to hybridisation are shown in the figure, along

with a colour legend. Green indicates issue-free plating of the island on both the ASIC and sensor sides. Brown indicates the absence of ENIG bumps on the island. Orange indicates a cut connection line. Light pink indicates shorted pixels, while dark pink indicates shorted connection lines for the corresponding island.



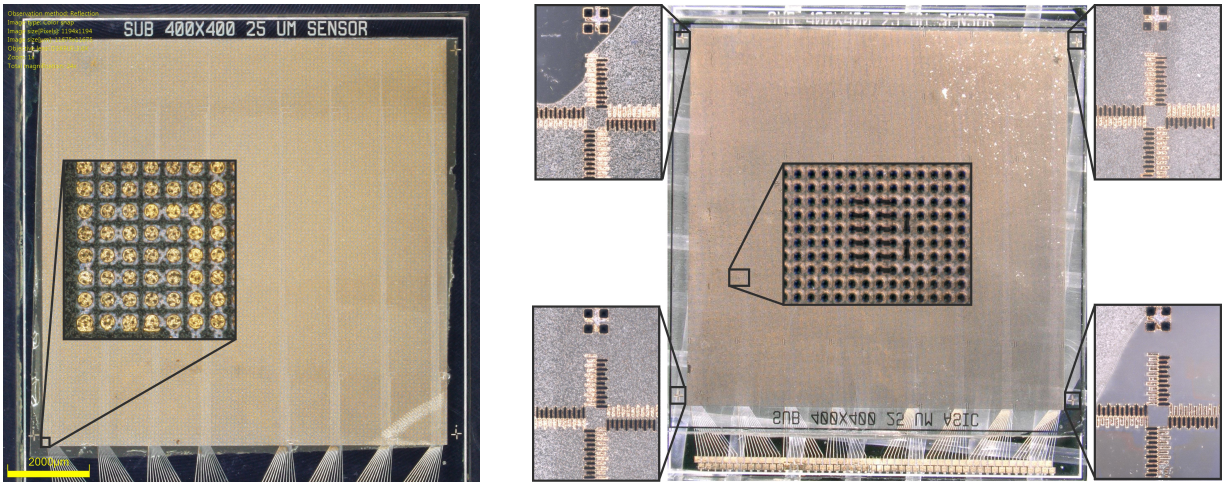
(a) Colour Legend (b) Assembly 1: 3.26a and 3.26f (c) Assembly 2: 3.26b and 3.26g

(d) Assembly 3: 3.26c and 3.26h (e) Assembly 4: 3.26d and 3.26i (f) Assembly 5: 3.26e and 3.26j

Figure 3.28: Information about the quality of the ENIG plating of the islands per assembly, obtained through the inspection of the chips before hybridisation.

All ten chips were cleaned with argon plasma for ten minutes prior to hybridisation. Hybridisation was carried out in two steps. First, the ACF was cut manually to the size of the matrix, using a razor blade. The ACF was then attached to the sensor side using a flip-chip machine (lamination). Lamination was performed at a force of 3,5 kgf and a temperature of 80 °C for all assemblies. Figure 3.29a shows the sensor side of Assembly 5 after lamination. The ACF appears as a yellowish rectangle on the matrix. The inlet shows an enlarged view of the first island at the bottom left of the chip.

The ENIG bumps are golden, and the connecting aluminium lines between electrically connected pixels appear silver coloured. The black dots, which are particularly visible on the ENIG bumps, are conductive micro-particles. On average, there are 3–4 particles on each ENIG bump.
Assemblies 1–3 were hybridised under the same conditions: a force of 75 kgf and a temperature of 210 °C. The hybridisations took place on different days. Assemblies 4 and 5 were performed on the same day as assembly 3, but the force was increased to 100 kgf for assembly 4. For assembly 5, the force was increased to 100 kgf and the temperature profile was adjusted. Rather than heating directly to 210 °C, the temperature was slowly increased to 70 °C over 5 minutes, then to 80 °C over 10 minutes, and finally to 210 °C. This gave the viscous ACF time to spread into the free volume between the ENIG bumps before it cures.
Figure 3.29b shows Assembly 5 after hybridisation. The inlets in the corners show the alignment crosses, while the inlet in the middle shows an island. The alignment crosses reveal an offset of 4 µm to the left and 5 µm downwards. The ENIG bumps on the top chip appear as black



(a) Sensor side of Assembly 5 after lamination. (b) Assembly 5 after hybridisation.

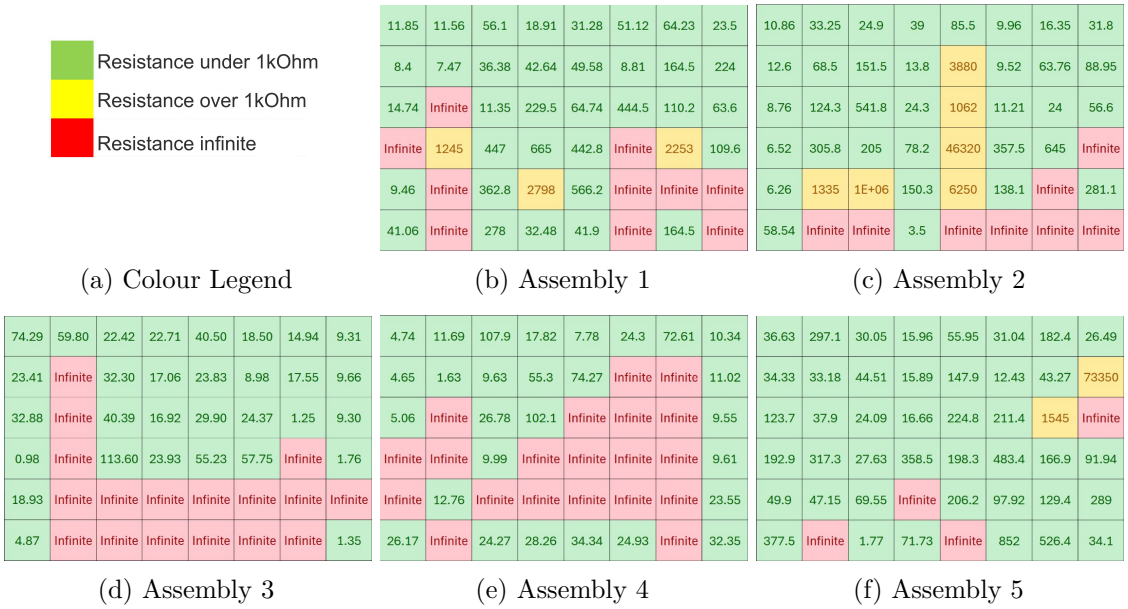
Figure 3.29: Images of Assembly 5 after lamination and after hybridisation.

areas. Due to the offset, the golden ENIG bumps on the bottom chip can be seen. The effect is enhanced by the design, which features narrower bumps on the top chip. The offset reduces the area in which micro-particles can get trapped. However, a good overlap of the ENIG bumps of the lower and upper chips is still visible.
Similar systematic offsets were observed for all assemblies after hybridisation. Assembly 1 had an offset of 3 µm to the left and 5 µm upwards. Assembly 2 had an offset of 2 µm to the left and 3 µm upwards. Assembly 3 had an offset of 5 µm to the left and 1 µm upwards. Assembly 4 had an offset of 1 µm to the left and 4 µm upwards. The offsets may be caused by high temperatures during bonding, which result in thermal expansion of the machine components, or by an uncalibrated machine.

3.4.3 Functional measurements

Subsequently, the functionality of the islands in all assemblies was measured using the probe station and measurement procedure described in section 2.2. Figure 3.30 shows the raw measurement results from the probe station as resistance in ohms. This resistance includes that of the cabling and probe needles, the contact between the needles and the contact pads, the connection lines, and the connection-chain through the island. Measurements with a resistance below 1 kΩ are marked in green and those above 1 kΩ are marked yellow. Yellow islands have an unusually high resistance, indicating poor electrical contact. Those marked in red have infinite resistance and are therefore not connected either in at least one of the 28 connections or have an interrupted connection line, meaning that no current can flow.

To estimate the resistance caused by hybridisation using conductive particles, the resistance of the probe needles and cabling, the resistance of the contact between the needles and the contact pads, and the resistance of the connection lines were determined. To measure the resistance of the needles and cabling and the resistance of the needle contact, the needles were placed close



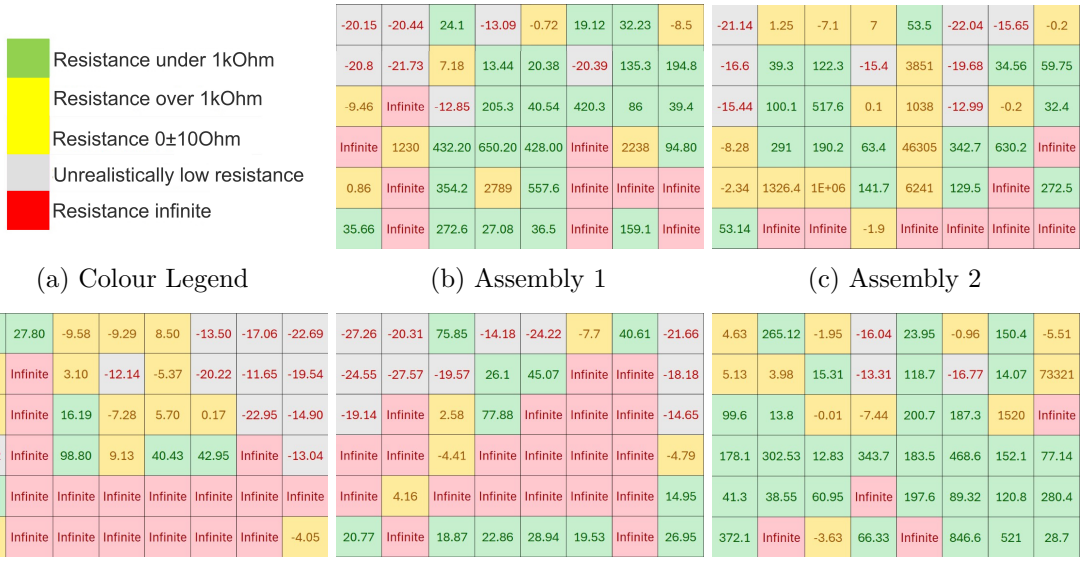
(a) Colour Legend (b) Assembly 1 (c) Assembly 2

(d) Assembly 3 (e) Assembly 4 (f) Assembly 5

Figure 3.30: Electrical resistance measurements of all islands in ohms and the arrangement of the islands and their resistances in a schematic representation for each assembly.

together on the same contact pad. This process was repeated several times, resulting in an average resistance of approximately 2 Ω. The connection lines vary in length depending on the position of the islands within the matrix. Those at the bottom of the matrix have short connection lines, and the length increases with height in the matrix. To measure this resistance, one needle was positioned on the ENIG bumps at the end of the connection line and the other one on the contact pad. A plated spare sample was used for this purpose. The resulting values were 3.7 Ω for the lowest islands, 5.3 Ω for the second row of islands, 8.4 Ω for the third row of islands, 13.1 Ω for the fourth row of islands, 15.6 Ω for the fifth row of islands, and 17 Ω for the sixth row of islands. These measurements include the resistance of the probe needles and cabling and the contact resistance of the needles. Since the contact lines lead up and down, the resistance must be doubled and the resistance of the needles and cabling and the needle contact must be subtracted once. The resulting resistance values for the probe needles and cabling plus the connection lines are 5.4 Ω, 8.6 Ω, 14.8 Ω, 24.2 Ω, 29.2 Ω and 32 Ω.

The raw measurement result from Figure 3.30 includes all the resistances listed above, as well as the island resistance. To make the island resistances comparable, the determined parasitic resistance values for the probe needles and cabling, needle contact and connection line must be subtracted. Figure 3.31 shows the estimated resistance values after subtracting these parasitic resistances. Two reasons for negative resistance values are considered.
Firstly, the resistance may be lower because a short in the connection line reduces the current path. In this case, the measured current does not flow through the micro-particles, but rather through this short circuit in the connection line.
The second possibility is that the resistance measurements for the probe station, needle contact and connection line vary depending on the island. In this case, a small negative result could still indicate a functioning island. Additionally, there could be islands where the access resistance



(a) Colour Legend

-20.15	-20.44	24.1	-13.09	-0.72	19.12	32.23	-8.5
-20.8	-21.73	7.18	13.44	20.38	-20.39	135.3	194.8
-9.46	Infinite	-12.85	205.3	40.54	420.3	86	39.4
Infinite	1230	432.20	650.20	428.00	Infinite	2238	94.80
0.86	Infinite	354.2	2789	557.6	Infinite	Infinite	Infinite
35.66	Infinite	272.6	27.08	36.5	Infinite	159.1	Infinite

(b) Assembly 1

-21.14	1.25	-7.1	7	53.5	-22.04	-15.65	-0.2
-16.6	39.3	122.3	-15.4	3851	-19.68	34.56	59.75
-15.44	100.1	517.6	0.1	1038	-12.99	-0.2	32.4
-8.28	291	190.2	63.4	46305	342.7	630.2	Infinite
-2.34	1326.4	1E+06	141.7	6241	129.5	Infinite	272.5
53.14	Infinite	Infinite	-1.9	Infinite	Infinite	Infinite	Infinite

(c) Assembly 2

42.29	27.80	-9.58	-9.29	8.50	-13.50	-17.06	-22.69
-5.79	Infinite	3.10	-12.14	-5.37	-20.22	-11.65	-19.54
8.68	Infinite	16.19	-7.28	5.70	0.17	-22.95	-14.90
-13.82	Infinite	98.80	9.13	40.43	42.95	Infinite	-13.04
10.33	Infinite	Infinite	Infinite	Infinite	Infinite	Infinite	Infinite
-0.53	Infinite	Infinite	Infinite	Infinite	Infinite	Infinite	-4.05

(d) Assembly 3

-27.26	-20.31	75.85	-14.18	-24.22	-7.7	40.61	-21.66
-24.55	-27.57	-19.57	26.1	45.07	Infinite	Infinite	-18.18
-19.14	Infinite	2.58	77.88	Infinite	Infinite	Infinite	-14.65
Infinite	Infinite	-4.41	Infinite	Infinite	Infinite	Infinite	-4.79
Infinite	4.16	Infinite	Infinite	Infinite	Infinite	Infinite	14.95
20.77	Infinite	18.87	22.86	28.94	19.53	Infinite	26.95

(e) Assembly 4

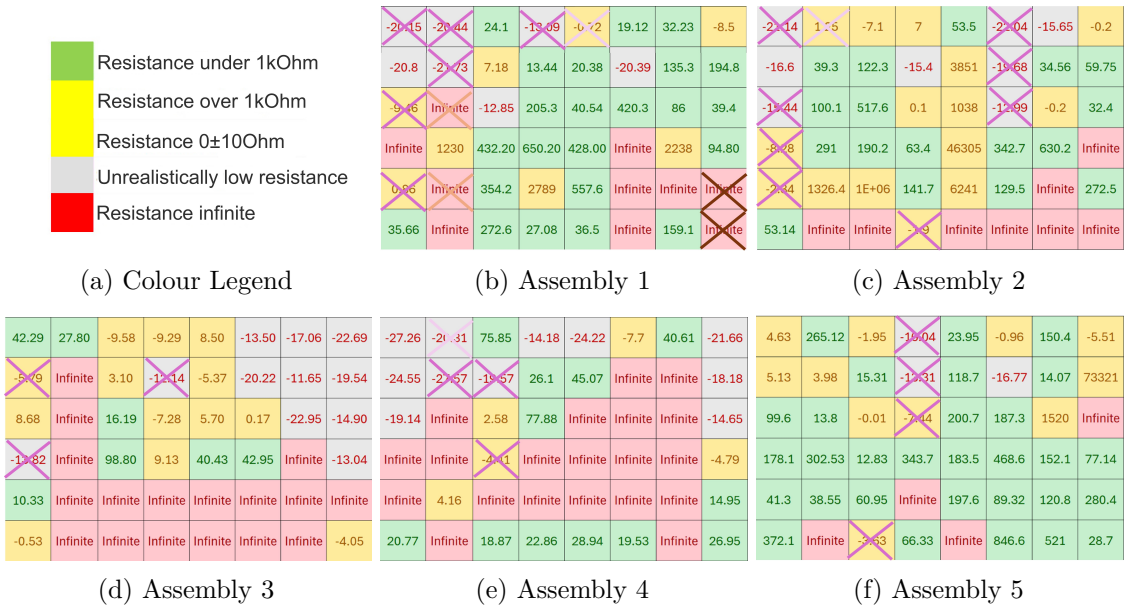
4.63	265.12	-1.95	-16.04	23.95	-0.96	150.4	-5.51
5.13	3.98	15.31	-13.31	118.7	-16.77	14.07	73321
99.6	13.8	-0.01	-7.44	200.7	187.3	1520	Infinite
178.1	302.53	12.83	343.7	183.5	468.6	152.1	77.14
41.3	38.55	60.95	Infinite	197.6	89.32	120.8	280.4
372.1	Infinite	-3.63	66.33	Infinite	846.6	521	28.7

(f) Assembly 5

Figure 3.31: Estimated electrical resistance values inside the island chains, obtained by subtracting the resistances for the probe needles and cabling, the needle contact, and the resistance of the connection lines.

exceeds the reference measurements and there is a short circuit in the connection line close to the island. Accordingly, there is an uncertainty about the functionality of islands with resistance values close to zero.
To account for the difference in negative resistance values and the uncertainty concerning low positive resistance values, resistance values ranging from -10 Ω to +10 Ω are marked in yellow in Figure 3.31, while stronger negative values are marked in grey. Values greater than +10 Ω but less than 1 kΩ are marked in green. Values above 1 kΩ are yellow and infinite resistance values are red. This results in four different interpretations of the islands. Grey islands are assumed to have a short circuit in the connection lines because the resistance is too low. Green islands are assumed to be fully functional, connected only by micro-particles. Red islands are assumed to have at least one dysfunctional pixel contact. Yellow islands are those where it is unclear whether they are functioning or not. To take this into account, best-case and worst-case interpretations are carried out later, in which all yellow islands are assumed to be functioning or not functioning respectively.
As the islands were visually examined in detail prior to hybridisation, the results can be compared with the measured and corrected resistance values from Figure 3.31. This is illustrated in Figure 3.32, where the information is transferred to the corresponding islands using coloured crosses with the same colour legend from Figure 3.28.

Prior to hybridisation, two islands with shorted connection lines (orange crosses) and two islands without ENIG bumps (brown crosses) were identified for Assembly 1. This inevitably results in non-functional islands. This is also confirmed by electrical measurements. The locations marked with orange and brown crosses in Figure 3.32b also have a red background, which indicates an absence of electrical contact.



(a) Colour Legend (b) Assembly 1 (c) Assembly 2

(d) Assembly 3 (e) Assembly 4 (f) Assembly 5

Figure 3.32: Corrected electrical resistances and coloured crosses indicating problematic islands before hybridisation. The colour legend for the crosses is the same as in Figure 3.28.

Light pink crosses indicate islands where shorted pixels were previously identified. This is the case for one island in each of assemblies 1, 2 and 4. Consequently, the resistance may be lower than that achieved through hybridisation with micro-particles. Electrical resistance measurements confirm this. With resistance values of -0.72 Ω, 1.25 Ω and -20.31 Ω, the resistance is either negative or very low. Such low values indicate electrical contact through the shorted pixels rather than through the micro-particles.
Dark pink crosses represent the last category of problematic islands observed before hybridisation. These indicate shorted connection lines, the most common issue arising after the ENIG process. Twenty-three of the 240 islands have shorted connection lines. The majority of these (16 in total) are found in the upper half of the matrixes. The probability of a short is greater for the islands in the upper half due to their longer connection lines. All dark pink crosses are located on grey or yellow backgrounds. Due to the shorted connection lines, the resistance is either strongly negative if the short is close to the connection pads (grey) or close to zero if it is close to an island (yellow). Taking into account the islands that were already problematic prior to hybridisation, there are two expected outcomes for the remaining islands (without crosses). Either hybridisation was successful, resulting in green islands, or it was unsuccessful, resulting in red islands with no electrical contact. However, the results show a third outcome involving grey and yellow backgrounds. These islands exhibit low or negative resistances, similar to islands with shorted connection lines.
One possible explanation is that micro-particles caused the connection lines to short during hybridisation. Since the test chips have a passivation problem that leads to parasitic ENIG plating at the edges, and since the connection lines are designed to be only 5 µm apart, it is possible that the 3 µm micro-particles could cause a short circuit in the presence of parasitic ENIG plating. This assumption is supported by the fact that most of the islands that are potentially shorted through hybridisation (grey islands without a cross) are located in the upper half of the matrix and are therefore more likely to experience this effect.

3.4.4 Estimation of interconnect yield

Assuming that the probability of successful connection remains consistent throughout the matrix and that there are no systematic issues, such as non-planarity of the flip-chip machine, leaving entire areas unconnected, the probability of connection can be calculated using the equation:

$$\frac{N_{\text{functional chains}}}{N_{\text{total chains}}} = P_{\text{functional chain}} = p_{\text{single connection}}^{N_{\text{connections per chain}}} \tag{3.1}$$

The probability for a functional island can be calculated based on the proportion of functional islands and the total number of islands. At the same time, the probability of a functional island can be determined by taking the probability for one functional connection to the power of the number of connections per island. Equation 3.1 can be rearranged to calculate the probability of a single functional connection:

$$p_{\text{single connection}} = \left(\frac{N_{\text{functional chains}}}{N_{\text{total chains}}}\right)^{\frac{1}{N_{\text{connections per chain}}}} \tag{3.2}$$

Using a worst-case scenario, only green islands are considered functional. There are 48 islands in total per assembly and 28 connections per island. Islands identified as problematic during visual inspection prior to hybridization are not included in the calculation, which reduces the total number of islands. The resulting probabilities for a single functional connection are 98.3% for assembly 1, 97.1% for assembly 2, 93.6% for assembly 3, 95.5% for assembly 4, and 98.6% for assembly 5.
In a best-case scenario, the islands for which it is unclear whether they are functional or not (yellow with no crosses) are also considered functional. This yields higher connection probabilities for a single functional connection of 99.0% for assemblies 1, 98.1% for assembly 2, 97.0% for assembly 3, 96.4% for assembly 4 and 99.8% for assembly 5.
Assemblies 1–3 were hybridised using the same parameters. The estimated connection yield varies by approximately 5% between the assemblies. Assembly 5 has the best connection yield and shows significantly more green fields in Figure 3.32 than the other assemblies. Therefore, the increased hybridisation time at lower temperatures in the beginning used for this assembly could be advantageous. More samples need to be examined to validate this conclusion.
The measurement results for the five assemblies demonstrate that hybridisation results require good control on ENIG plating of the individual chips and on the bonding parameters. The estimated high connection yield of up to 99% already demonstrates the potential of ENIG in combination with ACA for large-area fine-pitch hybridisation.

4 Conclusions and Outlook

This thesis presented a systematic parameter-optimization study for a selective ENIG process for pixel-detector hybridization with conductive adhesives.
Section 3.1 demonstrated that pretreatment significantly affects the quality of the ENIG plating. Multiple zincations can produce a more homogeneous ENIG layer with greater uniformity. This is evident in the SEM images and the optical height and AFM measurements. These results also align with those reported in other studies [36, 37, 38, 39, 40]. Multiple zincations should not only lead to greater uniformity but also to increased reliability of solder joints when ENIG is to be used as UBM for solder bumping [36].
Section 3.2 examined nickel deposition in more detail. The growth of nickel depends strongly on the temperature, pH value and stabiliser concentration parameters. This also explains why the reported rates for nickel growth vary depending on the study [41, 42, 43, 44]. The same applies to other parameters, such as nickel concentration. Qiao et al. [41] have built a special deposition tank for this reason, with sensors that precisely monitor all parameters to ensure consistent growth and predictable ENIG plating.
In addition, the effect of parasitic ENIG plating through pinholes was observed. This increases the probability of shorts occurring before and during hybridisation, and is therefore undesirable. Arshad et al. [42] also observed this effect and discovered that these parasitic ENIG spheres could be removed from the samples using ultrasound. Several other studies highlight the importance of the passivation layer in preventing nickel growth through pinholes [45, 46, 47, 48]. To provide additional protection from parasitic ENIG plating, a mask can be used during deposition [49, 50]. Such a mask also enables ENIG columns to be created, allowing for even smaller pitches to be plated. Tian et al. [49] exploited this to create ENIG columns with a height of 4 µm and a pitch of 8 µm. However, this makes the process more complex and less flexible.
Section 3.4 examined the potential of hybridisation with ENIG in combination with ACA bonding. A connection yield of up to 99% was estimated for test chips with a pitch of 25 µm and a matrix size of 400x400 pixels. No literature from other working groups could be found to verify the connection yield of ENIG and ACA. Furthermore, most studies on ENIG are conducted on chips with significantly larger pitches and pixel pads [35, 37, 51]. This thesis therefore highlights the potential for chips with small pitches.
To achieve connection yields close to 100%, several improvements are required. Firstly, the ENIG plating must be flawless across the entire matrix. While this is already achieved for functional chips with good passivation layers [3, 19], it is not guaranteed for the test chips used in this thesis. Secondly, the post-bonding alignment accuracy must be improved to ensure greater overlap of the ENIG bumps on the upper and lower chips. For future test chips, the gap between connection lines should be increased, to avoid potential shorts. Furthermore, the quality of the passivation must be improved to reduce parasitic ENIG growth. Improving these aspects and standardising the process will enable ENIG to be used in combination with ACA to produce hybrid assemblies consistently with high connection yield. Due to its flexibility and adaptability to different requirements, ENIG

offers a cost-effective alternative to solder bump bonding, particularly for smaller quantities in the research and development phase.

List of Figures

1.1 Schematic image of a hybrid pixel detector consisting of a silicon sensor on top bump-bonded to a readout ASIC below. The hybrid of sensor and ASIC is wire-bonded onto a "Motherboard" PCB. From [8]. 4
1.2 Schematic representation of hybrid pixel sensors using different hybridisation methods. 5
1.3 SEM images of solder bumps on a Timepix3 ASIC. 6
1.4 Images of the used flip-chip machine for this thesis and an example solder bump connection after hybridisation. 6
1.5 Images of copper pillars. 7
1.6 Schematic representations of ACA and the resulting electrical contact. 8
1.7 Schematic representation (cross-section view) of a sensor or ASIC pixel containing surface contamination. 9
1.8 Schematic representation of treatment with plasma. 10
1.9 Schematic representation of etching of the aluminium and the deposition of zinc. 10
1.10 Schematic representation of nickel deposition. 11
1.11 Schematic representation of immersion gold bath. 11

2.1 Dimensions and positioning of the individual devices on the wafer, as well as an actual image of the wafer after manufacture [22]. 12
2.2 Visualisation of the design of the two matching devices. 13
2.3 Visualisation of individual islands of the two daisy chain devices. 13
2.4 Schematic representation of the island after hybridisation, the resulting chain and the electrical connection shown as a red line. 14
2.5 Various equipment used for the sample preparation and inspections. 15
2.6 Equipments used for the sample inspections. 16
2.7 Setups used for this thesis for the entire ENIG process. 17
2.8 Process workflow for generating txt-files for height measurements. 18
2.9 Display of the GUI of the custom developed analysis software. 19

3.1 SEM image of one of the six samples and corresponding EDS analysis showing the composition of elements on the sample surface. 20
3.2 Measurements of the roughness of the exposed aluminium on all six samples and exemplary SEM image of one pad from sample 6. 21
3.3 SEM image of Sample 2 after Pretreatment and corresponding EDS analysis. . . 22
3.4 SEM images of samples 1-6 after their respective pretreatment. 23
3.5 Measurements of the roughness of the pad of all six samples after pretreatment (orange) and before pretreatment (grey). The picture inlets show the corresponding SEM images of samples 2, 4 and 6 after the respective pretreatment steps. 24
3.6 SEM image of Sample 6 after ENIG and corresponding EDS analysis. 25

3.7 SEM images of samples 1-6 after their respective pretreatment followed by ENIG deposition with the same parameters used for all samples. 26
3.8 Measurements of the roughness of the pad of all six samples after ENIG (green), after pretreatment (orange) and before pretreatment (grey). The picture inlets show the corresponding SEM images of samples 2, 4 and 6 after ENIG. 27
3.9 AFM measurements of samples 2, 4 and 6 after ENIG on a 10μmx10μm square area on the bonding pads, in top view with height scale (a, c and e) and in 3D visualisation (b, d and f). 28
3.10 Light microscope images of the five samples: before treatment (a–e); after pretreatment with three zincations (f–j); and after the ENIG process for 10, 20, 30, 40 or 50 minutes (k–o). Images of the samples after pretreatment and after the ENIG process also include a zoomed-in view showing individual pixels. 30
3.11 Height measurements and SEM images of the plating series under standard conditions (85°C, pH = 4.8, 200 μl/l stabiliser) with different deposition times for the five samples. 31
3.12 Schematic representation of nickel growth through a pinhole over time. 32
3.13 SEM images of the position where the sample was examined for pinholes, as well as the direction in which the material was removed using the FIB. 32
3.14 SEM images after FIB cross-section showing the pinholes in the passivation. Figures a and b show cross-sections taken at position 1, while figures c and d show cross-sections taken at position 2. 33
3.15 FIB cross-section taken at a different position, examining an ENIG sphere between two ENIG bumps. 34
3.16 Plating series with reduced and increased temperatures during deposition and different deposition times. 35
3.17 Plating series with reduced and increased pH value during deposition and different deposition times. 36
3.18 Plating series with reduced and increased stabiliser concentration during deposition and different deposition times. 37
3.19 Schematic representation and comparison of nickel growth through pinholes and nickel growth starting on the passivation layer. 37
3.20 SEM images showing nickel deposition on the passivation layer of samples with stabiliser concentration of 0μl/l. 38
3.21 SEM images showing nickel deposition stopping at the edge of the contact pads in the periphery, for samples with a stabiliser concentration of 400 μl/l. 38
3.22 Plating series with increased temperature and pH value during deposition and different deposition times. 39
3.23 Plating series for all the above parameters. 40
3.24 Absolute standard deviation of the height values of the samples that were plated with different parameters. 41
3.25 Relative standard deviation of the height values of the samples that were plated with different parameters. 42
3.26 Light microscope images of the five 'SUB 400x400 25UM ASIC' in (a)-(e) and the five 'SUB 400x400 25UM Sensor' in (f)-(j) after the ENIG process. 43
3.27 The categories into which the examined islands and connection lines were sorted, along with example images of each category. 44

3.28 Information about the quality of the ENIG plating of the islands per assembly, obtained through the inspection of the chips before hybridisation. 45
3.29 Images of Assembly 5 after lamination and after hybridisation. 46
3.30 Electrical resistance measurements of all islands in ohms and the arrangement of the islands and their resistances in a schematic representation for each assembly. 47
3.31 Estimated electrical resistance values inside the island chains, obtained by subtracting the resistances for the probe needles and cabling, the needle contact, and the resistance of the connection lines. 48
3.32 Corrected electrical resistances and coloured crosses indicating problematic islands before hybridisation. The colour legend for the crosses is the same as in Figure 3.28. 49

List of Tables

3.1 Pretreatment step, Make-up solution and parameter 22
3.2 ENIG steps, Make-up solutions and parameters 24
3.3 Make-up solution for nickel deposition 29
3.4 Make-up solution for immersion gold 29

Bibliography

[1] Frank Hartmann. *Evolution of Silicon Sensor Technology in Particle Physics*, volume 275 of *Springer Tracts in Modern Physics*. Springer, 2017. (cited on page 3)

[2] Conny Hansson and Krzysztof Iniewski, editors. *X-ray photon processing detectors*. Springer International Publishing, Cham, 2024. (cited on page 3)

[3] Haripriya Bangaru, Giovanni Calderini, Dominik Dannheim, Rui De Oliveira, Ahmet Lale, Moritz Lauser, Mateus Vicente Barreto Pinto, and Peter Svihra. High density hybridisation using enig bumping and anisotropic conductive films, 2025. (cited on the pages 3, 43, and 51)

[4] ep-dep.web.cern.ch. https://ep-dep.web.cern.ch/rd-experimental-technologies. [Accessed 16-12-2025]. (cited on page 3)

[5] Home | DRD3 - R&D on Semiconductor Detectors — drd3.web.cern.ch. https://drd3.web.cern.ch/. [Accessed 16-12-2025]. (cited on page 3)

[6] Home | AIDAinnova — aidainnova.web.cern.ch. https://aidainnova.web.cern.ch/. [Accessed 16-12-2025]. (cited on page 3)

[7] Hermann Kolanoski and Norbert Wermes. *Teilchendetektoren*. Springer, Berlin, Germany, 1 edition, March 2016. (cited on page 4)

[8] M Platkevic. *Signal processing and data read-out from position sensitive pixel detectors*. PhD thesis, Ph. D. Thesis, Czech Technical University in Prague, 2014. (cited on the pages 4 and 53)

[9] Xin Wu, Xueqi Zhu, Shuaishuai Wang, Xuehuang Tang, Taifu Lang, Victor Belyaev, Aslan Abduev, Alexander Kazak, Chang Lin, Qun Yan, and Jie Sun. Bump-Fabrication Technologies for Micro-LED Display : A Review. (Lcd):1–30, 2025. (cited on page 5)

[10] Yang Si, ShunHu Yang, YuNa Shi, Wen Wang, YongLiang Li, QiongFang Wang, ChaoWei Yang, DaFan Zuo, YuanQing Feng, GuiQin Zhao, YanZhen Liu, XiangQian Wang, XiongJun Li, and ShouZhang Yuan. Fabrication of high-aspect-ratio 5 m ultra-small pitch indium bump arrays by vacuum thermal deposition under variable rate. *Infrared Physics Technology*, 148:105869, 2025. (cited on the pages 5 and 7)

[11] L. F. Miller. Controlled collapse reflow chip joining. *IBM Journal of Research and Development*, 13(3):239–250, 1969. (cited on page 6)

[12] Alan Huffman, Richard Labennett, Salvatore Bonafede, and Chad Statler. Eutectic Sn / Pb Fine-Pitch Solder Bumping and Assembly for Rad-Hard Pixel Detectors. (May):1–12, 2002. (cited on page 6)

[13] P. Svihra, J. Braach, E. Buschmann, D. Dannheim, K. Dort, T. Fritzsch, H. Kristiansen, M. Rothermund, J.V. Schmidt, M. Vicente Barreto Pinto, and M. Williams. Development of novel single-die hybridisation processes for small-pitch pixel detectors. *Journal of Instrumentation*, 18(03):C03008, mar 2023. (cited on page 7)

[14] P Soussan, B Majeed, P Le Boterf, and P Bouillon. 2015-ECTC-Evaluation-of-Sn-Based-µbump.pdf. pages 597–602, 2015. (cited on page 7)

[15] Aibin Yu, John H. Lau, Soon Wee Ho, Aditya Kumar, Wai Yin Hnin, Da Quan Yu, Ming Ching Jong, Vaidyanathan Kripesh, Damaruganath Pinjala, and Dim Lee Kwong. Study of 15μm pitch solder microbumps for 3D IC integration. *Proceedings - Electronic Components and Technology Conference*, (July 2015):6–10, 2009. (cited on page 7)

[16] Robert Wilder — linkedin.com. https://h7.cl/1f-eU. [Accessed 10-12-2025]. (cited on page 8)

[17] Hannele Heikkinen, Akiko Gädda, Sami Vähänen, Jaakko Salonen, Philippe Monnoyer, Gabriel Blaj, Lukas Tlustos, and Michael Campbell. Low-temperature bump bonding of timepix readout chips and cdte sensors at different sensor pitches. In *2011 IEEE Nuclear Science Symposium Conference Record*, pages 4770–4775, 2011. (cited on page 9)

[18] Alexander Volker, Janis Viktor Schmidt, Dominik Dannheim, Peter Svihra, Mateus Vicente Barreto Pinto, Rui de Oliveira, Justus Braach, Xiao Yang, Marie Ruat, Débora Magalhaes, Matteo Centis Vignali, Giovanni Calderini, and Helge Kristiansen. Pixel detector hybridisation and integration with anisotropic conductive adhesives. *Journal of Instrumentation*, 19(5), 2024. (cited on page 11)

[19] Haripriya Bangaru, Giovanni Calderini, Dominik Dannheim, Rui De Oliveira, Ahmet Lale, Mateus Vicente Barreto Pinto, Janis Viktor Schmidt, Peter Svihra, Matteo Centis Vignali, Alexander Volker, and Xiao Yang. Pixel detector hybridization at low temperature with adhesives. *Journal of Instrumentation*, 20(7), 2025. (cited on the pages 11 and 51)

[20] Haripriya Bangaru, Giovanni Calderini, Dominik Dannheim, Yahya Khwaira, Helge Kristiansen, Ahmet Lale, Rui De Oliveira, Mateus Vicente Barreto Pinto, Petra Riedler, Janis Viktor Schmidt, Peter Svihra, Matteo Centis Vignali, Alexander Volker, and Xiao Yang. Development of in-house plating and hybridisation technologies for hybrid pixel detectors. *Journal of Instrumentation*, 20(7), 2025. (cited on page 11)

[21] J. V. Schmidt, J. Braach, D. Dannheim, R. De Oliveira, P. Svihra, and M. Vicente Barreto Pinto. Pixel detector hybridisation with anisotropic conductive films. *Journal of Instrumentation*, 18(1), 2023. (cited on page 11)

[22] AIDAinnova Completion of planar sensor production for ACF. 4:1–9, 2022. (cited on the pages 12 and 53)

[23] Laser unit | NMP Website — nmp.fcbg.ch. https://nmp.fcbg.ch/home/laser-unit/. [Accessed 10-12-2025]. (cited on the pages 14 and 15)

[24] HPT-300 & HPT-500 - Henniker Plasma — plasmatreatment.co.uk. https://h7.cl/1f-fa. [Accessed 10-12-2025]. (cited on page 15)

[25] Digitalmikroskop VHX-6000 von KEYENCE | KEYENCE Deutschland — keyence.de. https://www.keyence.de/landing/lpc/vhx6000.jsp. [Accessed 10-12-2025]. (cited on page 15)

[26] Hitachi High-Tech Corporation. Scanning Electron Microscope FlexSEM 1000 II : Hitachi High-Tech Corporation — hitachi-hightech.com. https://www.hitachi-hightech.com/global/en/products/microscopes/sem-tem-stem/sem/flexsem1000.html. [Accessed 10-12-2025]. (cited on page 15)

[27] ContourX-100 — bruker.com. https://www.bruker.com/en/products-and-solutions/test-and-measurement/3d-optical-profilers/contourx-100.html. [Accessed 10-12-2025]. (cited on page 16)

[28] Dimension Icon AFM — bruker.com. https://rb.gy/xam0nu. [Accessed 16-12-2025]. (cited on page 16)

[29] Focused Ion Beam - Scanning Electron Microscopy (FIB-SEM) | EN-MME-MM — en-mme-mm.web.cern.ch. https://en-mme-mm.web.cern.ch/content/focused-ion-beam-scanning-electron-microscopy-fib-sem. [Accessed 16-12-2025]. (cited on page 16)

[30] Accμra100 – SET. [Accessed 16-12-2025]. (cited on page 16)

[31] Atotech - Leading Plating Technologies — atotech.com. https://www.atotech.com/. [Accessed 16-12-2025]. (cited on page 18)

[32] AI Assistant Cursor — cursor.com. https://cursor.com/. [Accessed 16-12-2025]. (cited on page 18)

[33] Gwyddion Free data analysis software — gwyddion.net. https://gwyddion.net/. [Accessed 16-12-2025]. (cited on page 18)

[34] M. K. Md Arshad, A. Jalar, and I. Ahmad. Characterization of parasitic residual deposition on passivation layer in electroless nickel immersion gold process. *Microelectronics Reliability*, 47(7):1120–1126, 2007. (cited on page 32)

[35] S. Vähänen, T. Tick, and M. Campbell. Low-cost bump bonding activities at CERN. *Journal of Instrumentation*, 5(11), 2010. (cited on the pages 32 and 51)

[36] Siti Hajar Abdullah, Ibrahim Ahmad, and Azman Jalar. The effect of number of zincation in Electroless Nickel Immersion Gold (ENIG) Under Bump Metallurgy (UBM) on reliability in microelectronics packaging. *2006 25th International Conference on Microelectronics, MIEL 2006 - Proceedings*, (Miel):567–570, 2006. (cited on page 51)

[37] Rosine Coq Germanicus, Philippe Leclère, Eric Hug, Florent Lallemand, and Philippe Descamps. Statistical investigations of an ENIG Nickel film morphology by Atomic Force Microscopy. *E3S Web of Conferences*, 12:1–6, 2016. (cited on page 51)

[38] Hossein Ahmadian, Tianfeng Zhou, Weijia Guo, Qian Yu, A. M. Sadoun, A. Fathy, Yang Xuanzhe, and M. Elmahdy. Influence of initial surface roughness on the deposition and adhesion of electroless Ni-P plating on 6H-SiC substrate. *Results in Engineering*, 25(December 2024):103891, 2025. (cited on page 51)

[39] Mohd Khairuddin Md Arshad, Ibrahim Ahmad, Azman Jalar, and Ghazali Omar. The effects of zincation process on aluminum bond pad surfaces for Electroless Nickel Immersion Gold (ENIG) deposition. *Proceedings ICSE 2004 - 2004 IEEE International Conference on Semiconductor Electronics*, 00(c):656–662, 2004. (cited on page 51)

[40] Yu Yang, Jian Cai, Shuidi Wang, and Songliang Jia. The impact of zincation on the electroless nickel UBM for low cost flip chip technology. *2005 6th International Conference on Electronics Packaging Technology*, 2005:229–233, 2005. (cited on page 51)

[41] Yingtai Qiao, Jian Hou, Min Lai, and Fengzhou Fang. Control system and process optimization for electroless nickel plating. *Nanotechnology and Precision Engineering*, 8(2), 2025. (cited on page 51)

[42] Mohd Khairuddin Md Arshad, Ibrahim Ahmad, Azman Jalar, and Ghazali Omar. The surface characteristics of under bump metallurgy (UBM) in electroless nickel immersion gold (ENIG) deposition. *Microelectronics Reliability*, 46(2-4):367–379, 2006. (cited on page 51)

[43] Zaliman Sauli, Vithyacharan Retnasamy, Fairul Afzal Ahmad Fuad, Phaklen Ehkan, and Muhamad Hafiz Ab Aziz. Relationship between controllable process parameters on bump height in ENIG. *Applied Mechanics and Materials*, 404:62–66, 2013. (cited on page 51)

[44] Vithyacharan Retnasamy, Zaliman Sauli, Uda Hashim, Aaron Koay Terr Yeow, Steven Taniselass, and Ramzan Mat Ayub. Chemical bath temperature investigation for electroless nickel immersion gold. *Advanced Materials Research*, 925:96–100, 2014. (cited on page 51)

[45] Thomas Oppert, Thorsten Teutsch, and E. Zakel. A roadmap to low cost flip chip technology and chip size packaging using electroless nickel gold bumping. 01 1998. (cited on page 51)

[46] Thomas Oppert, E. Zakel, and Thorsten Teutsch. A roadmap to low cost flip chip and csp using electroless ni/au. pages 106 – 113, 05 1998. (cited on page 51)

[47] Congzhi Liu, D.A. Hutt, David Whalley, Paul Conway, and Samjid Mannan. Under bump metallisation of fine pitch flip-chip using electroless nickel deposition. volume 10, pages 64 – 71, 02 2000. (cited on page 51)

[48] Thomas Oppert, Thorsten Teutsch, and E. Zakel. Low cost flip chip bumping. pages 72 – 78, 02 2000. (cited on page 51)

[49] Liang Tian, Chang Lin, Kui Pan, Yu Lu, Liying Deng, Zhonghang Huang, Tianxi Yang, Yongai Zhang, Jie Sun, and Qun Yan. Electroless Deposition of 4 μm High Ni/Au Bumps for 8 μm Pitch Interconnection. *ACS Applied Electronic Materials*, 4(10):4966–4971, 2022. (cited on page 51)

[50] Yu Lu, Chang Lin, Shuaishuai Wang, Kaixin Zhang, Taifu Lang, Yang Li, Qiwei Li, Tianxi Yang, Zhonghang Huang, Chunli Yan, Jie Sun, and Qun Yan. Electroless deposition of nickel microbumps for fine-pith flip-chip bonding. *Journal of Physics: Conference Series*, 2783(1), 2024. (cited on page 51)

[51] Véronique Vitry, Joachim Hastir, Alexandre Mégret, Sepehr Yazdani, Muslum Yunacti, and Luiza Bonin. Recent advances in electroless nickel-boron coatings. *Surface and Coatings Technology*, 429(August 2021), 2022. (cited on page 51)